Resource

Cell Reports

Rotational trophoblast organoids reveal biomechanical regulation of trophoblast differentiation

Graphical abstract

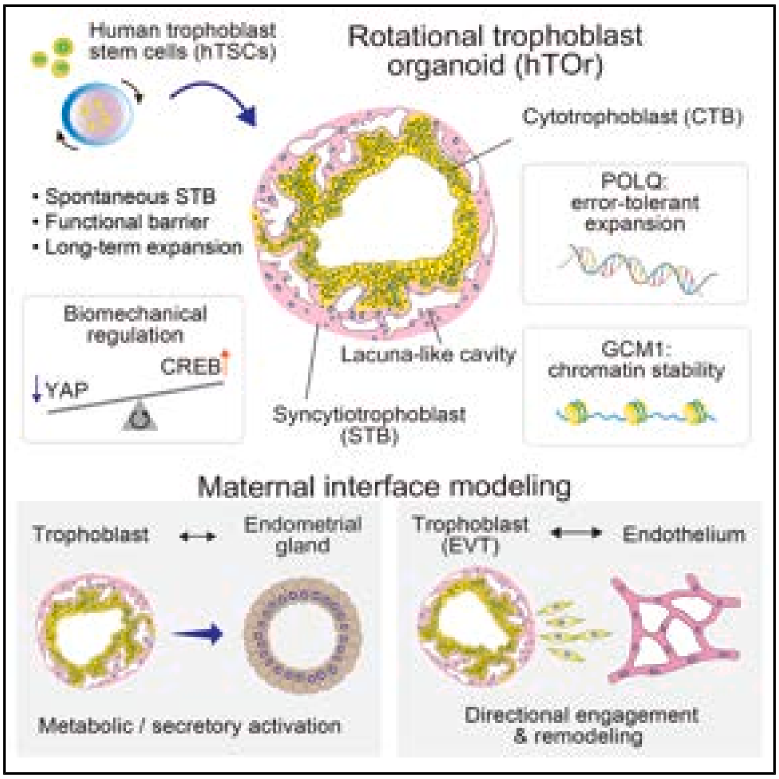

Highlights

- Matrix-free rotation generates polarized human trophoblast organoids
- Biomechanical YAP-CREB balance promotes outer syncytiotrophoblast specification
- POLQ supports error-tolerant expansion while GCM1 stabilizes chromatin state
- Organoids model trophoblast-endometrial and trophoblast-endothelial interactions

Authors

Shun Shibata, Yuki Ishikawa, Marina Kosaka, Hiroaki Okae, Takahiro Arima

Correspondence

shun.shibata.a3@tohoku.ac.jp

In brief

Shibata et al. develop a rotational platform that generates polarized human trophoblast organoids with extensive outer syncytiotrophoblast, lacunae-like cavities, and a functional diffusion barrier. A biomechanical YAP–CREB balance, POLQ-supported genome maintenance, and GCM1-mediated chromatin stabilization regulate trophoblast development, and the system enables modeling of maternal interface interactions.

Shibata et al., 2026, Cell Reports *45*, 117637
July 28, 2026 © 2026 The Author(s). Published by Elsevier Inc.
https://doi.org/10.1016/j.celrep.2026.117637

Cell Reports

CellPress
OPEN ACCESS

Resource

Rotational trophoblast organoids reveal biomechanical regulation of trophoblast differentiation

Shun Shibata,[1,2,5,*] Yuki Ishikawa,[1] Marina Kosaka,[1] Hiroaki Okae,[3] and Takahiro Arima[1,4]

[1]Department of Informative Genetics, Environment and Genome Research Center, Tohoku University Graduate School of Medicine, Sendai 980-8575, Japan
[2]Research and Development Division, Rohto Pharmaceutical Co., Ltd., Osaka 544-8666, Japan
[3]Department of Trophoblast Research, Institute of Molecular Embryology and Genetics, Kumamoto University, Kumamoto 862-0973, Japan
[4]Institute of Development, Aging and Cancer, Tohoku University, Sendai 980-8575, Japan
[5]Lead contact
*Correspondence: shun.shibata.a3@tohoku.ac.jp

https://doi.org/10.1016/j.celrep.2026.117637

SUMMARY

Human placental development is essential for pregnancy but remains mechanistically obscure because early post-implantation tissues are inaccessible. Here, we establish a rotational trophoblast organoid platform that recapitulates selected morphogenetic features shared with early trophoblast development, including spontaneous syncytiotrophoblast (STB) differentiation and progressive fusion of lacuna-like cavities. Integrated multi-omic analyses associate this architecture with a biomechanical balance between attenuated YAP activity and peripheral CREB activation, with GCM1 stabilizing trophoblast chromatin state and POLQ supporting genome maintenance in rapidly expanding progenitors. The organoids display autonomous endocrine activity, induce an endometrial epithelial state consistent with metabolic activation, and can generate extravillous trophoblasts that directionally engage endothelial networks. This platform provides a framework for studying placental morphogenesis and tissue interactions relevant to pregnancy complications.

INTRODUCTION

The human placenta mediates maternal-fetal exchange and hormone production essential for pregnancy.[1–3] Post-implantation, the trophectoderm differentiates into a primitive syncytium that erodes maternal capillaries to establish lacunae—precursors of the intervillous space.[4–7] Underlying cytotrophoblasts (CTBs) then proliferate to form primary villi, which mature into functional exchange units as extraembryonic mesenchymal cells infiltrate the villous core to form secondary villi, followed by vasculogenesis to create tertiary villi.[8] Despite their importance, the mechanistic understanding of these events remains limited because early tissues are inaccessible and, in many countries, research on human embryos *in vitro* is legally restricted to 14 days of development.[9–11]

To bridge this gap, stem cell-based models have emerged. Human trophoblast stem cells (hTSCs)[12] and organoids derived from primary tissue[13,14] or hTSCs[15] have provided valuable tools. However, recent benchmarking highlights significant limitations, particularly for hTSC-derived models, which may exhibit transcriptomic misalignments or lineage biases compared to primary tissue.[16,17] Furthermore, current organoid systems face architectural constraints: Matrigel-embedded cultures typically exhibit inverted polarity with internal syncytiotrophoblasts (STBs), while suspension methods often yield simple aggregates lacking complex morphogenetic features.[18–20] Most existing systems lack stromal and endothelial villous-core components and therefore miss reciprocal signaling during villous assembly.

Here, we establish a rotational culture platform for the scalable generation of genetically tractable human trophoblast organoids (hTOrs). Using this system, we map trophoblast state transitions during early morphogenesis, identify a role for POLQ in genome maintenance during progenitor expansion, and examine how YAP-associated biomechanical cues and GCM1-associated chromatin regulation shape differentiation. We further show that hTOr exhibits endocrine activity and interacts with endometrial epithelium and endothelial networks. This platform enables mechanistic studies of human placental morphogenesis and tissue interactions.

RESULTS

Generation of scalable rotational trophoblast organoids modeling early placental morphogenesis and barrier function

To model early placental morphogenesis, we generated hTSC spheroids in ECSY medium.[21] Dropout analysis identified CHIR99021, SB202190, and Y27632 as indispensable for aggregation, while EGF was retained to align with standard

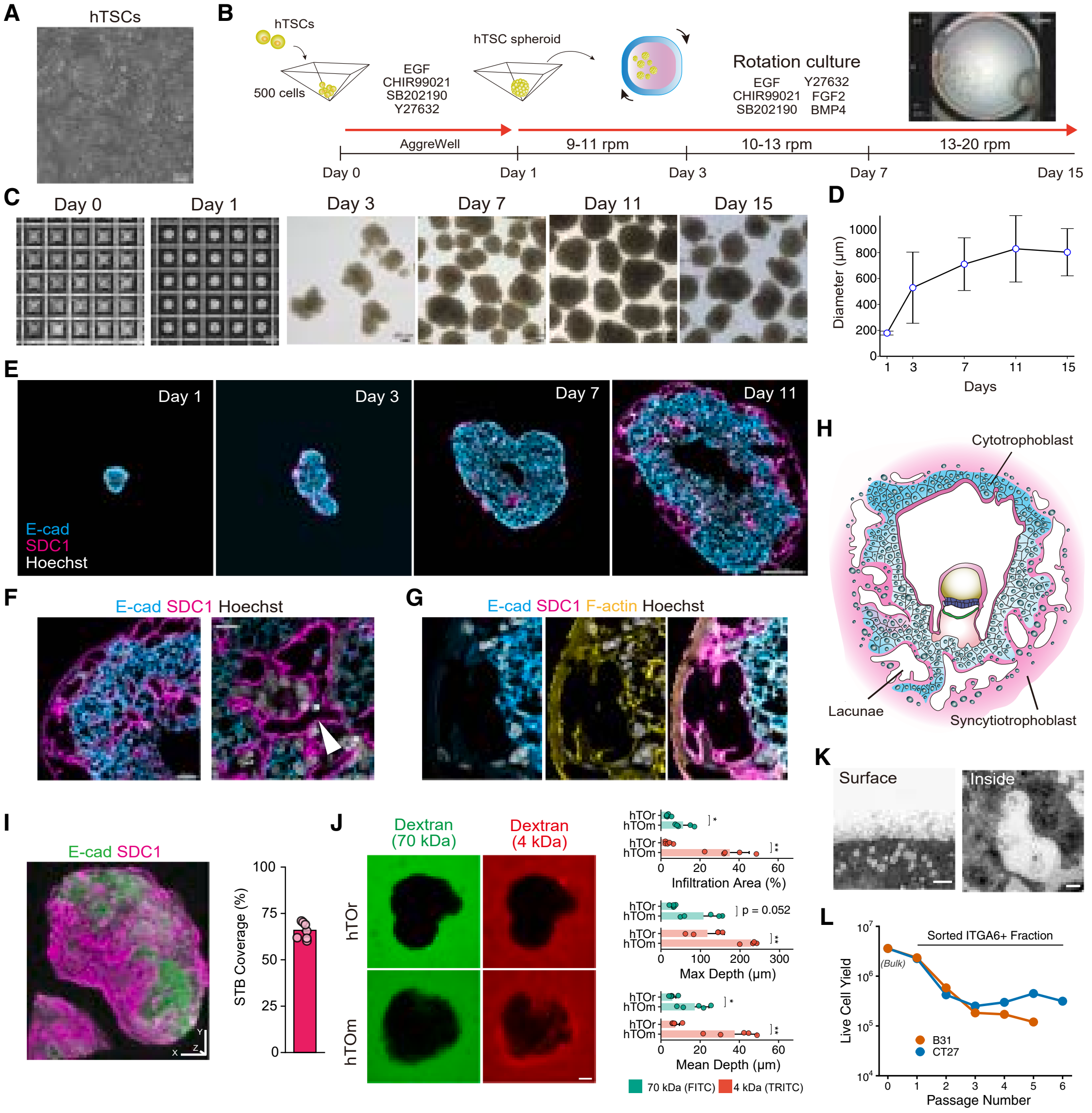

Figure 1. Generation of scalable rotational trophoblast organoids modeling early placental morphogenesis and barrier function

(A) Phase-contrast image of cultured hTSCs. Scale bars, 200 μm.

(B) Schematic of the hTOr generation protocol.

(C) Time-course images of spheroid formation and morphological development during rotational culture. Scale bars, 200 μm.

(D) Maximum organoid diameter over time. Mean ± SD (n = 62, 24, 49, 60, and 58 organoids for days 1, 3, 7, 11, and 15; 4 independent experiments).

(E) Immunofluorescence of developing hTOr. Cyan: E-cad; magenta: SDC1; white: nuclei. Scale bars, 200 μm.

(F and G) Day 11 hTOr shows the outer SDC1$^+$ STB layer and internal lacuna-like cavities (F, white arrowhead) and cell fusion with F-actin remodeling (G). Cyan: E-cad; magenta: SDC1; yellow: F-actin; white: nuclei. Scale bars, 100 and 20 μm (F), 20 μm (G).

(H) Schematic of post-implantation human embryo architecture (approx. day 14), based on anatomical descriptions in the Carnegie Atlas[22] and Hertig et al.[23]

(I) 3D reconstruction (left) and quantification (right) of SDC1$^+$ STB surface coverage. Mean ± SD (n = 7 organoids, 3 experiments). Scale indicator, 100 μm.

(J) Dextran permeability assay compares hTOr and hTOm (Matrigel). 70 kDa FITC-dextran (green) and 4 kDa TRITC-dextran (red). Quantification of Infiltration Area, Max Depth, and Mean Depth. Mean ± SD (n = 5 organoids). *$p < 0.05$ and **$p < 0.01$ by unpaired two-tailed *t* test. Scale bars, 100 μm.

(K) TEM shows microvilli on the organoid surface and internal structures. Scale bars, 2 μm (left) and 5 μm (right).

(L) Expansion kinetics of sorted ITGA6$^+$ progenitors over serial passages (P1–P6) versus bulk seeding (P0).

See also Figure S1.

trophoblast organoid protocols[13,14] (Figure S1A). Following microwell aggregation, spheroids were transitioned to a rotational culture system supplemented with BMP4 and FGF2[18] (Figures 1A and 1B). Under these dynamic conditions, hTSC spheroids fused and expanded ~4-fold, reaching ~800 μm in diameter by day 11 (Figures 1C and 1D).

Temporal analysis revealed the progressive expansion of Syndecan-1 (SDC1)$^+$ STB cells, both at the organoid periphery and within the interior (Figure 1E). High-resolution imaging captured extensive STB domains at the organoid periphery alongside internal lacuna-like cavities (Figure 1F). Active syncytialization involved dynamic cytoskeletal remodeling, with cortical actin reorganization and F-actin extension from the plasma membrane into the cytoplasm during fusion (Figure 1G). Aspects of this organization recall early post-implantation trophoblast architecture (Figure 1H).[7,22,23]

Quantitative whole-mount imaging demonstrated that these outer SDC1$^+$ domains cover 65.6 ± 4.5% of the total surface area (Figure 1I). Analysis of representative organoids at sequential time points visualized the progressive fusion of internal lacuna-like cavities (Figure S1B). High-resolution 3D imaging captured structural intermediates of this process, revealing STB bridges separating adjacent lacuna-like cavities prior to fusion (Figure S1C). Ultimately, syncytial fusion drives the continuous expansion of the internal lumen area (Figure S1D). To distinguish active morphogenetic remodeling from necrosis-driven cavitation, we quantified apoptosis via cleaved caspase-3 staining. Apoptosis rates remained negligible (<1.5%) through day 11, confirming that initial lumen formation and expansion are driven by active morphogenesis rather than consequences of cell death (Figure S1E). Functional integrity was further validated by dextran exclusion assays; unlike barrier-compromised hTOrs cultured in Matrigel (hTOm), hTOr effectively excluded both 4 kDa and 70 kDa dextrans (Figure 1J), demonstrating that the outer STB domain functions as a physical diffusion barrier.

Ultrastructural analysis supported functional maturation, revealing dense microvilli on both exterior and internal STB surfaces (Figure 1K). Furthermore, to assess long-term expandability, we established a passaging protocol based on ITGA6$^+$ progenitor selection (Figure S1F). This strategy enabled 5–6 passages (up to 102 days) without exhaustion, supporting sustained self-renewal (Figures 1L and S1G). Thus, the hTOr system models specific spatial and morphogenetic aspects of early trophoblast development—including spontaneous STB differentiation and the progressive fusion of lacuna-like cavities—while providing a scalable and robust platform.

Single-nucleus profiling delineates trophoblast hierarchies and POLQ-mediated genomic safeguarding

To dissect these cellular dynamics, we performed single-nucleus RNA-seq (snRNA-seq) on day-11 hTOr. Unsupervised clustering identified five transcriptionally distinct trophoblast populations (Figure 2A). Based on canonical marker expression (Figure 2B) and label transfer to an *in vivo* ref.[25] (Figure S2A), we annotated (CTB; *TP63*$^+$) and highly proliferative CTB (pCTB; *MKI67*$^+$). Additionally, we identified a transitional *GCM1*$^+$ population[26] (CTB-fusing), which progressed into STB defined by robust *PSG3* and *ERVW-1* expression (Figure S2B). Notably, an *ITGA2*$^+$/*IGFBP3*$^+$ cluster exhibited minimal *HLA-G* expression, consistent with proximal column CTBs (villous CTB column subset, VCT-CCC) in the reference atlas (Figure S2C). Accordingly, we designated this population as column CTBs (cCTBs), representing the proximal progenitor pool for the extravillous lineage. Immunofluorescence confirmed the localization of ITGA2$^+$ cells directly beneath the outer STB, consistent with a column-base progenitor identity (Figure S2D). RNA velocity analysis delineated distinct lineage trajectories, revealing that cCTBs primarily originate from the pCTB pool, whereas STB differentiation proceeds through a CTB intermediate and the *GCM1*$^+$ fusing state (Figure 2C). Gene ontology (GO) analysis confirmed functional specialization: The pCTB cluster was enriched for cell cycle processes (e.g., chromosome segregation, DNA replication), consistent with an actively cycling progenitor phenotype. In contrast, the cCTB cluster exhibited robust hypoxia response signatures (Figure 2D), reflecting adaptation to the proximal cell column niche. Differential expression analysis further validated these states, highlighting the enrichment of replication factors (*DIAPH3*, *POLQ*) in pCTBs relative to quiescent CTBs, and the induction of hypoxia-responsive/EVT-priming genes (*FLT1*, *IGFBP3*) as cells commit to the cCTB fate (Figure S2E).

To precisely determine the developmental stage of our model, we projected the single-nucleus data onto an extended human embryonic reference atlas (E5–E14 to First Trimester).[24] Quantitative projection analysis indicated that the majority of hTOr cells mapped to early embryonic reference populations: 81% of the TE/CTB lineage and 74% of STB mapped to the E5–E14 reference, consistent with shared transcriptional features between hTOr and early embryonic reference populations (Figures 2E and 2F,; S2F). Consistent with this early embryonic-like state, the STB cluster specifically enriched *MMP14* (MT1-MMP)—a key protease required for ECM degradation during early placentation[27]—while lacking late-gestation MMPs (Figure S2G). DQ-Gelatin assays confirmed functional proteolytic activity at the organoid surface (Figure S2H).

To characterize the transcriptional dynamics along this developmental continuum, we assigned a “maturation score” to each cell based on reference alignment (Figure 2G). Within the TE/CTB lineage, maturation positively correlated with the upregulation of nutrient transporters (*SLC43A2*) and cytoskeletal regulators (*VAV3*). Conversely, negatively correlated genes included cell cycle/DNA repair factors (*DIAPH3*, *POLQ*, *RRM2*, *ANLN*), reflecting a progressive exit from the highly proliferative progenitor state. In the STB lineage, maturation was marked by progressive induction of functional transporters (*SLC2A3*) and vascular signaling factors (*FLT1*) central to placental physiology.[28] Notably, early-stage STB maintained high expression of *RAP1B*, a regulator of invasion signaling,[29] and the polarity determinant *EXOC6B*.[30] This distinct early signature aligns with the dynamic cytoskeletal remodeling required for early trophoblast syncytialization, demonstrating that hTOr exhibit transcriptional programs associated with trophoblast maturation *in vivo*.

To dissect the upstream regulatory drivers of these transitions, we inferred transcription factor (TF) and signaling pathway activities (Figures 2H and S2I). In the TE/CTB lineage, maturation correlated with the downregulation of proliferation-driving TFs (e.g., E2F1–4, FOXM1, MYC) and a concomitant increase in p53 pathway activity, reflecting the transition toward quiescence and active DNA damage surveillance.[31] In contrast, STB maturation was defined by the activation of the ISGF3 complex (STAT1/2, IRF9), which establishes constitutive antiviral defenses.[32] Concurrently, Hypoxia and JAK-STAT pathways were upregulated in mature STBs, consistent with physiological adaptation

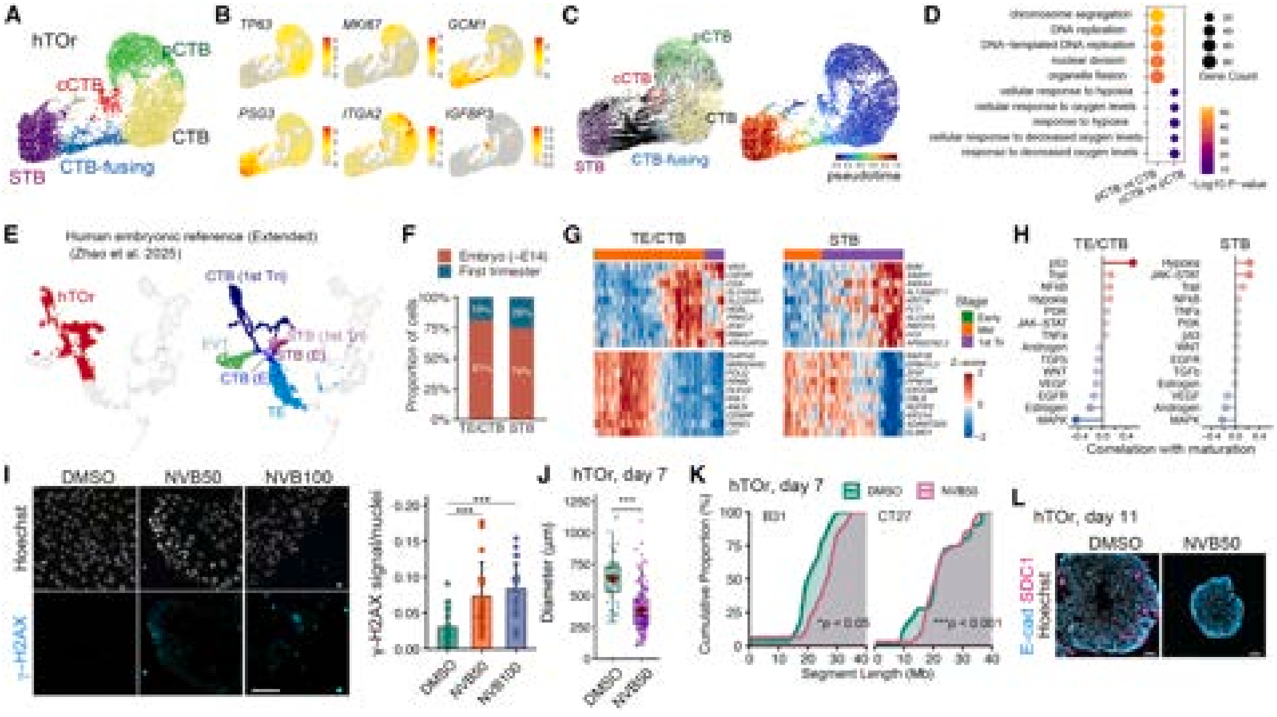

Figure 2. Single-nucleus profiling delineates trophoblast hierarchies and POLQ-mediated genomic safeguarding

(A) UMAP of day 11 hTOr identifying five populations: CTB, pCTB, cCTB, CTB-fusing, and STB.

(B) Expression of key marker genes. Color scale: gray (low) to red (high).

(C) RNA velocity (left) and pseudotime (right) delineating differentiation trajectories.

(D) GO (Biological Process) enrichment compares pCTB vs. CTB (left) and cCTB vs. pCTB (right). Dot size: gene count; color: $-\log_{10}$(adjusted p value).

(E) Projection of hTOr transcriptomes onto the extended human embryonic reference atlas.[24] Left: hTOr cells (red). Right: Reference cells colored by lineage and stage.

(F) Proportion of TE/CTB and STB lineages mapping to Embryonic (red) or First-Trimester (teal) reference populations.

(G) Smoothed expression of genes correlated with maturation score in TE/CTB (left) and STB (right). Color: Z score.

(H) Spearman correlation between PROGENy pathway scores and maturation score.

(I) γ-H2AX immunofluorescence of hTSCs treated with NVB for 24 h. Scale bars, 50 μm. Mean ± SD (n = 24, 25, and 25 images for Control, 50 μM, and 100 μM, analyzing 11,296, 9,823, and 10,021 nuclei; 2 experiments). ***$p < 0.001$ by Kruskal-Wallis test with Dunn's correction.

(J) Organoid diameter at day 7 after DMSO (n = 54) or NVB 50 μM (n = 132) treatment; 2 experiments. ***$p < 0.001$ by Welch's t test.

(K) Cumulative distribution of CNA segment lengths in B31 and CT27 lines treated with DMSO or NVB 50 μM for 7 days. Segment length indicates the genomic span of contiguous bins with similar copy-number states and is used here to describe the fragmentation of the copy-number landscape. n = 10,919/10,348 and 10,584/11,590 segments.

*$p < 0.05$ (B31) and ***$p < 0.001$ (CT27) by Kolmogorov-Smirnov test.

(L) Day 11 hTOr treated with DMSO or NVB 50 μM. Cyan: E-cad; magenta: SDC1; white: nuclei. Scale bars, 100 μm.

See also Figure S2.

to the hypoxic placental niche[33] and enhanced cytokine responsiveness. Furthermore, MAPK signaling progressively declined across both lineages, reflecting its transient role in initiating early differentiation.[34]

Strikingly, *POLQ* emerged as a hallmark of the early proliferative state; it was highly enriched in pCTBs and negatively correlated with maturation, indicating preferential expression in developmentally younger cells. *POLQ* encodes DNA polymerase theta, the central effector of theta-mediated end joining (TMEJ), which is critical for resolving replication-associated double-strand breaks (DSBs).[35] In hTOr, *POLQ* expression peaked during the S/G2M phases (Figure S2J), consistent with *in vivo* cycling trophoblasts[36] (Figure S2K). To functionally test its role, we inhibited POLQ using novobiocin (NVB).[37] In 2D hTSC cultures, NVB treatment triggered a marked accumulation of DSBs (γ-H2AX) and severe nuclear abnormalities, ultimately culminating in cell loss (Figure 2I and S2L–S2N). Extending this to the 3D hTOr system, POLQ inhibition significantly restricted organoid growth (Figure 2J). To assess the genomic consequences, shallow whole-genome sequencing revealed that NVB treatment shifted copy number alteration (CNA) segment lengths toward longer distributions and reduced genome-wide copy-number instability metrics, including median absolute deviation (MAD) scores and fraction of genome altered (FGA), in the surviving cells (Figures 2K and S2O). Segment length represents the genomic span of contiguous CNA regions and measures copy-number landscape fragmentation; MAD scores and FGA provide complementary measures of the amplitude and genomic extent of copy-number alterations, respectively. Structurally, NVB-treated organoids exhibited disrupted architecture at day 11, characterized by the failure to form coherent STB domains (Figure 2L). Together, these results suggest that POLQ enables rapid proliferation by tolerating replication stress via error-prone repair—generating short CNA segments at the expense of strict genomic fidelity. This trade-off between proliferative speed and genomic stability likely contributes to the pervasive placental mosaicism observed in humans.[38]

Rotational culture promotes trophoblast differentiation by modulating CREB/YAP balance

To define how culture modality governs differentiation, we compared rotational culture with static suspension (floating), horizontal agitation (shaking), and Matrigel embedding. While rotational and Matrigel conditions both supported growth (Figure S3A), their differentiation trajectories diverged: Only rotational culture yielded robust SDC1+ STB formation, whereas Matrigel-embedded spheroids remained undifferentiated (Figures 3A and 3B; S3B). Gene regulatory network (GRN) analysis identified CREB1 as a top-ranked hub specifically activated in rotational culture, anchoring an STB-functional module (Figure 3C). Notably, phosphorylated CREB (pCREB) was specifically localized to the organoid periphery under rotation but was absent in other modalities, linking hydrodynamic forces to surface-localized STB induction (Figures 3D and S3C).

Given the divergent transcriptomes, we hypothesized a role for mechanosensitive YAP signaling.[40–42] Indeed, Matrigel embedding maintained high nuclear YAP (∼85%) and robust YAP/TAZ transcriptional signatures,[39] whereas rotational culture attenuated nuclear YAP to ∼43% (Figures 3E and 3F; S3D). To establish causality, we induced constitutively active YAP (YAP5SA), which profoundly disrupted morphogenesis—yielding irregular, undifferentiated organoids lacking STB (Figures 3G and 3H; S3E and S3F). snRNA-seq confirmed the loss of STB identity and the emergence of a unique YAP-induced population characterized by high TEAD/MYC activity and the absence of canonical differentiation markers (Figures 3I; S3G and S3H). GRN analysis revealed that YAP5SA rewired the regulatory landscape, prioritizing a proliferative program at the expense of CREB1/FOXP-mediated differentiation (Figures 3J and S3I). Crucially, phase-space analysis showed that YAP5SA cells progressed along differentiation pseudotime without exiting the cell cycle, manifesting a "cycling differentiation" state driven by mitotic programs (Figures 3K and S3J). These effects were unique to 3D morphogenesis and absent in 2D growth (Figure S3K), underscoring the dimensionality-dependence of YAP function. Our results support a model (Figure 3L) where rotational culture coordinates STB differentiation by balancing peripheral CREB activation with reduced matrix-dependent YAP activity.

GCM1 stabilizes trophoblast chromatin state and restrains an ectopic pioneer-factor program

Beyond biomechanical cues, lineage specification is governed by the master regulator GCM1.[43] Recent work by Cinkornpumin et al. demonstrated that loss of GCM1 in hTSCs and organoids impairs differentiation and disrupts contact inhibition.[44] Building on these foundational findings, we investigated how GCM1 stabilizes trophoblast identity at the chromatin level in rotational organoids. To address this, we performed single-nucleus multiome profiling on *GCM1* KO hTOr engineered with a targeted deletion of exon 3, which encodes the DNA-binding domain (Figure 4A).[45] Consistent with the prior study, GCM1 deficiency abolished STB formation; however, in rotational culture, *GCM1* KO organoids yielded solid, undifferentiated structures with restricted diameter—a phenotype distinct from the "hollow ball" morphology reported under static suspension conditions[44] (Figures 4B and S4A). Multiome analysis confirmed the complete loss of mature STB populations (Figures 4C and S4B), and coverage analysis verified the efficient deletion of exon 3 in these KO samples (Figure S4C). These arrested cells remained locked in the active cell cycle (S/G2M) and accumulated proximal column markers (e.g., *ITGA2*) but failed to upregulate distal column/EVT-associated genes (e.g., *ITGA1*, *CDH5*) or progress toward the STB lineage (Figures S4D–S4F).

To elucidate the regulatory logic underlying this arrest, we analyzed TF binding dynamics through footprint deconvolution. GCM1 loss triggered a global reorganization of the TF landscape, where occupancy of differentiation drivers (GCM1, CEBPG, CREB1) collapsed, while KLF/MAZ-family factors gained *de novo* accessibility (Figures 4D; S4G and S4H). In control organoids, progressive chromatin accessibility for GCM1 and its co-factors was functionally coupled with target gene expression (Figures 4E and 4F). Conversely, *GCM1* KO organoids exhibited a destabilized progenitor landscape: pioneer factors (KLF4, KLF5, MAZ) and constitutively accessible factors (e.g., FOXN3) remained consistently accessible, whereas accessibility at a subset of TEAD4 motif-containing regions was reduced in *GCM1* KO organoids, suggesting a more complex relationship between GCM1 and YAP-TEAD-associated regulatory programs[40,46] (Figures S4I and S4J).

GRN analysis identified GATA6 as a prominent shared target of these pioneer and constitutively accessible factors (Figure 4G). Accordingly, *GATA6* expression was elevated in KO organoids (Figure 4H), supported by increased accessibility at the *GATA6* locus harboring binding motifs for KLF/MAZ (Figure 4I). This enhanced GATA6 motif accessibility was functionally coupled with the upregulation of its target genes (Figure S4K). Differential expression analysis confirmed that GATA6$^+$ subpopulations selectively activated an aberrant mesenchymal and stress-response program (e.g., Rho GTPase, TGF-β signaling) (Figures 4J and 4K), rather than a canonical primitive endoderm identity (Figure S4L). Together, our findings extend the recent GCM1 study by demonstrating that GCM1 enforces STB lineage fidelity by restraining opportunistic pioneer factors and preventing the ectopic activation of aberrant transcriptional programs.

Autonomous endocrine and paracrine functions of hTOr drive endometrial epithelial metabolic activation

Robust endocrine competence is a hallmark of mature trophoblasts. To assess hTOr functional maturation within the complex placental steroid biosynthetic pathways (Figure 5A), we profiled key regulatory enzymes. Single-nucleus transcriptomics revealed that rate-limiting enzymes for progesterone (CYP11A1, HSD3B1) and estrogen (CYP19A1) synthesis, along with the glucocorticoid barrier enzyme HSD11B2, were robustly enriched in the STB population (Figure 5B). Although lower, CYP17A1 and

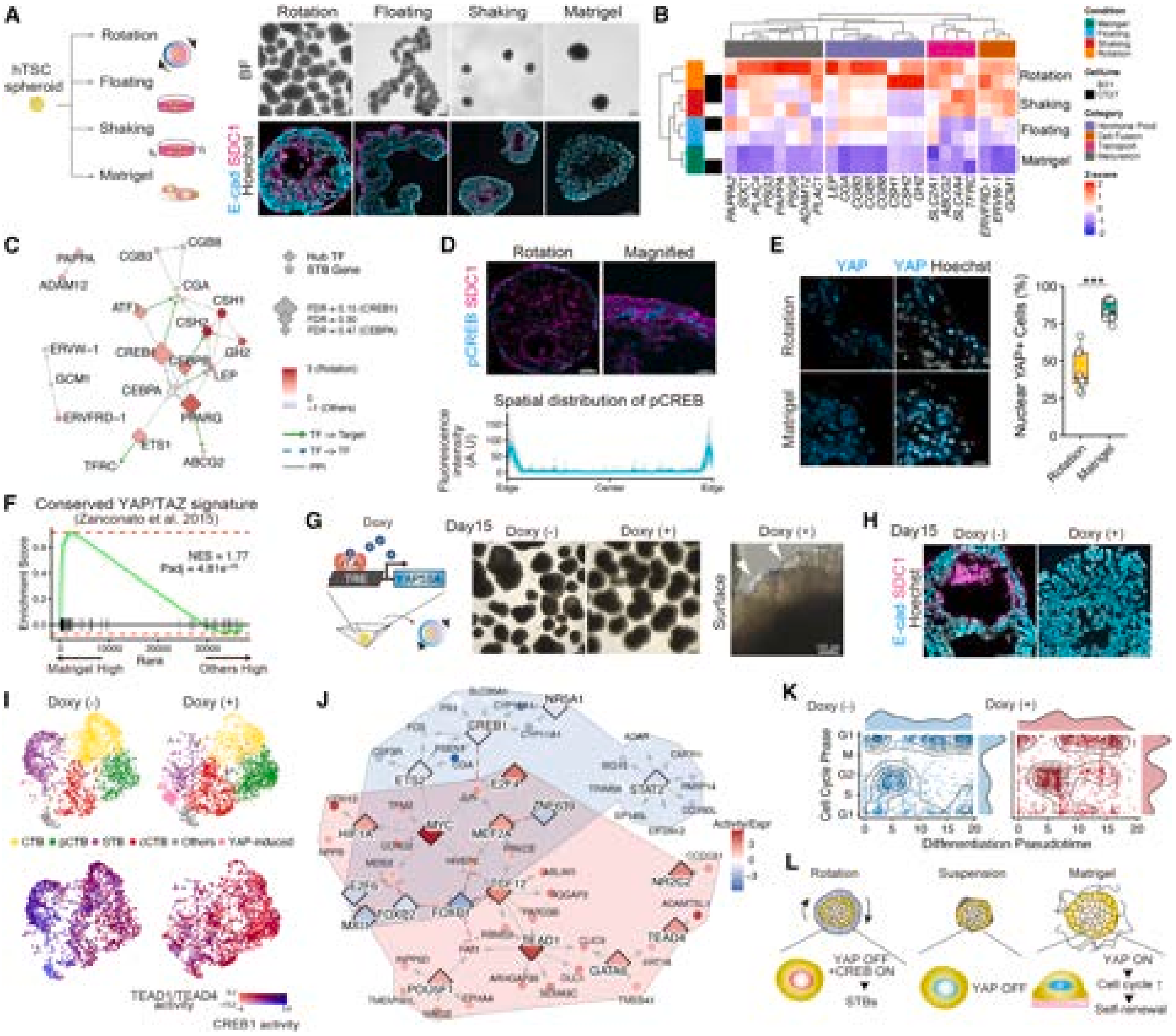

Figure 3. Rotational culture promotes trophoblast differentiation by modulating CREB/YAP balance

(A) Schematic (left) and images (right) of organoids under four culture conditions. Top: Brightfield. Bottom: Immunofluorescence for E-cad (cyan), SDC1 (magenta), nuclei (white). Scale bars, 500 μm (BF), 200 μm (IF).

(B) Z-scored expression of STB markers across conditions ($n = 2$ lines).

(C) Hub TF network regulating STB genes. Node size: significance; color: Rotation Dominance. Edges: DoRothEA (arrows) or STRINGdb (lines). Selection criteria: FDR <0.25 (VIPER/DoRothEA A–C); STRINGdb score >700.

(D) pCREB (cyan) and SDC1 (magenta) immunofluorescence (top) and spatial pCREB distribution across organoid diameter (bottom). Mean ± SD ($n = 10$ organoids).

(E) YAP immunofluorescence (cyan) in Rotation vs. Matrigel. Scale bars, 20 μm. Nuclear YAP quantification: median and quartiles ($n = 9$ organoids per group). $^{***}p < 0.001$ by Welch's t test.

(F) GSEA of "Conserved YAP/TAZ Signature"[39] in Matrigel vs. suspension cultures.

(G) Doxy-inducible YAP5SA system (left) and day 15 brightfield (right). Arrowheads: aberrant surface features. Scale bars, 500 μm, 100 μm (inset).

(H) Day 15 organoids. E-cad (cyan), SDC1 (magenta), nuclei (white). Scale bars, 200 μm.

(I) UMAP of control and YAP5SA organoids (top) and bivariate TEAD1/4 (red) vs. CREB1 (blue) activity (bottom).

(J) Force-directed GRN landscape. Node color indicates expression change (red: upregulated; blue: downregulated in YAP5SA). Shaded areas: YAP-Driven Proliferation Module (red) and Suppressed Differentiation Module (blue).

(K) Phase-space trajectory of pseudotime vs. cell cycle phase, showing decoupled "cycling differentiation" in YAP5SA.

(L) Proposed biomechanical balance model.

See also Figure S3.

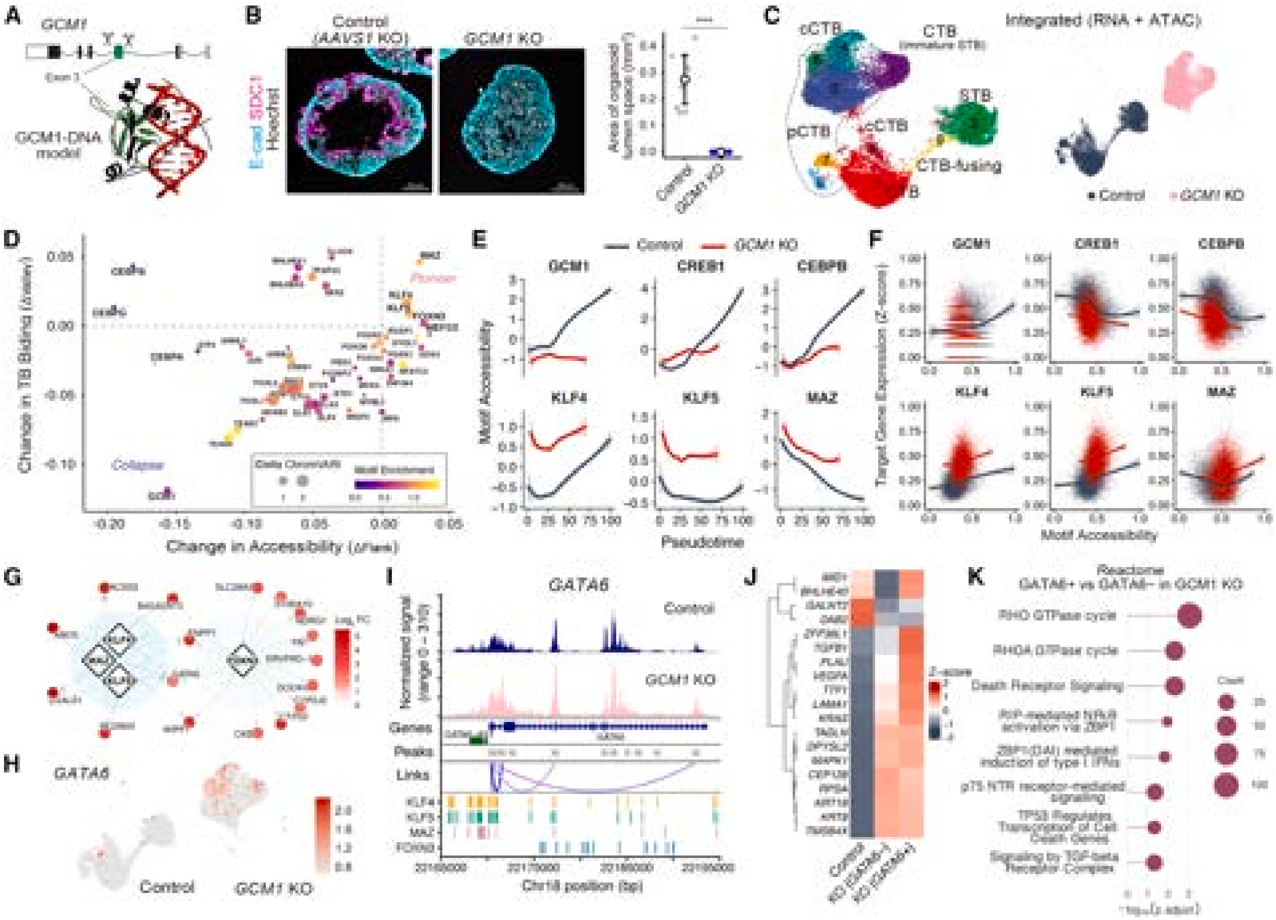

Figure 4. GCM1 stabilizes trophoblast chromatin state and restrains an ectopic pioneer-factor program

(A) CRISPR/Cas9 targeting of *GCM1* exon 3 (upper) and GCM1-DNA complex model[45] (lower).

(B) Day 11 organoid immunofluorescence (left) and internal lumen area quantification (right). Scale bars, 200 μm. Mean ± SD ($n = 8$ Control, $n = 7$ *GCM1* KO). $^{***}p < 0.001$ by Mann–Whitney U test.

(C) WNN-UMAP of multiome data identifying trophoblast populations (left) and split UMAP visualization by genotype (right; navy: Control, pink: *GCM1* KO).

(D) Footprint deconvolution separates DNA binding (ΔValley) from flanking accessibility (ΔFlank). Top-right "Pioneer" quadrant (MAZ, KLF4, KLF5): active remodeling; bottom-left "Collapse" quadrant: GCM1. Point size: |ΔChromVAR|; color: motif enrichment in KO-specific peaks.

(E) Motif accessibility along pseudotime. Differentiation drivers (top) open progressively in Control; Pioneer factors (bottom) remain accessible in KO. Shaded: 95% CI.

(F) TF motif accessibility vs. target expression at the single-cell level. LOESS regression lines shown.

(G) GRN of the ectopic pioneer program. Diamonds: driver TFs; circles: target genes. Color: $\log_2$FC.

(H) *GATA6* expression on UMAP.

(I) ATAC-seq coverage at the *GATA6* locus. KO (pink) vs. Control (navy), with pioneer factor motifs indicated.

(J) GATA6 target gene expression in control, KO (GATA6^-), and KO (GATA6^+). Color: *Z* score.

(K) Reactome enrichment of GATA6^+ vs. GATA6^- cells in KO organoids. Dot size: gene count.

See also Figure S4.

AKR1C family members remained detectably expressed (Figure S5A). Consistent with these transcriptional profiles, LC-MS/MS of culture supernatants detected key intermediates (pregnenolone, progesterone, estradiol) and confirmed functional cortisol-to-cortisone conversion. This was accompanied by the activation of neurosteroid and mineralocorticoid pathways, including deoxycorticosterone (DOC) and allopregnanolone (Figure 5C). Furthermore, hTOr produced a robust secretome characterized by high levels of hCG and diverse trophoblast-derived proteins (Figures S5B–S5D).

Beyond autonomous endocrine function, we sought to reconstruct the maternal-fetal interface. Upon co-embedding hTOr with GFP-expressing human endometrial organoids (hEMOs)[21] in Matrigel, direct contact induced localized epithelial thickening and folding (Figure 5D), significantly increasing epithelial height compared to non-contact controls (Figure 5E). High-throughput morphometric analysis revealed a striking distance-dependent remodeling gradient, where proximal hEMO exhibited progressive loss of their cystic lumen structure (Figures 5F and S5E). Congruently, hTOr-conditioned medium markedly upregulated

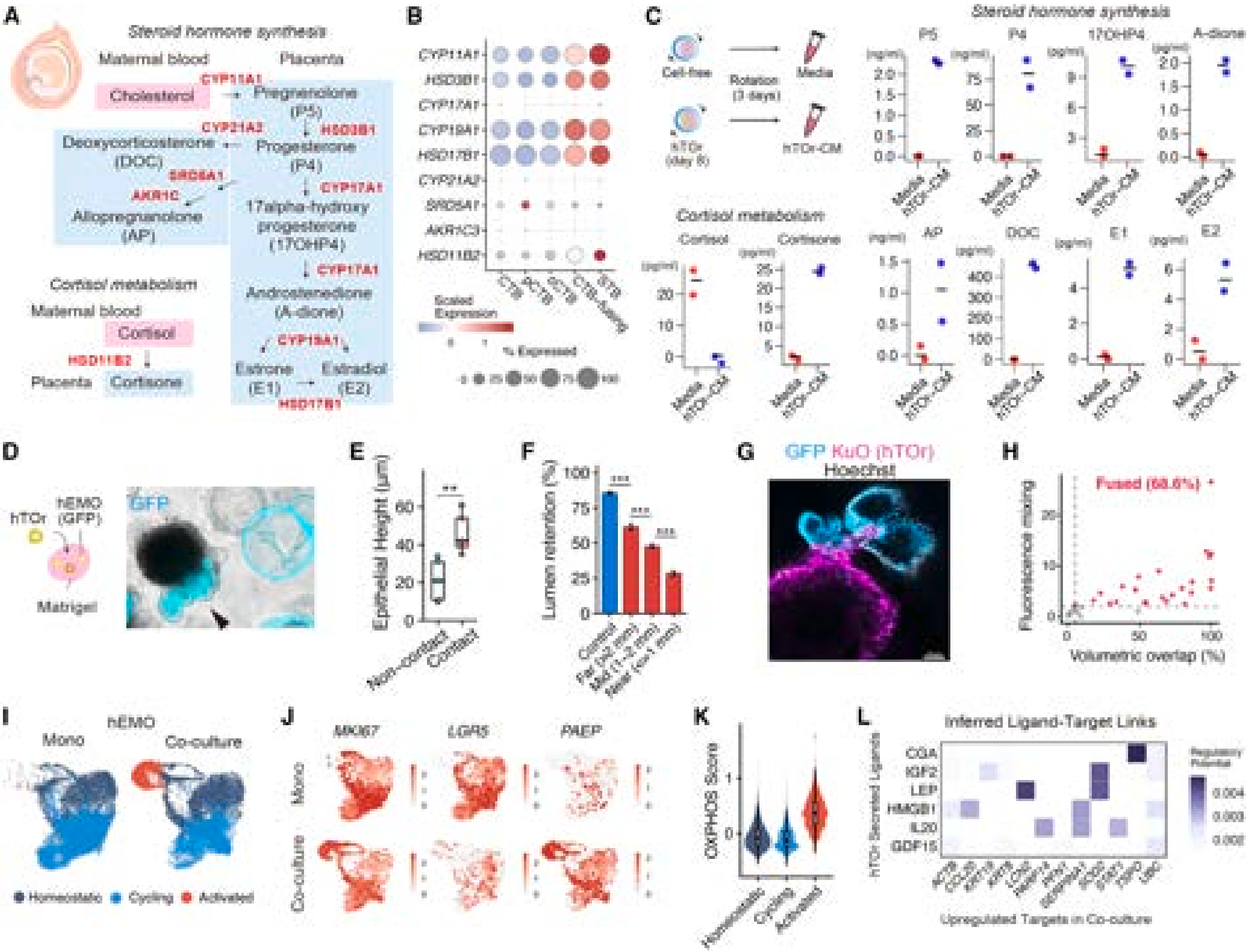

Figure 5. Autonomous endocrine and paracrine functions of hTOr drive endometrial epithelial metabolic activation

(A) Schematic of placental steroid hormone synthesis and cortisol metabolism pathways.

(B) Steroidogenic enzyme expression across trophoblast subpopulations. Dot size: percent expressed; color: scaled expression.

(C) LC-MS/MS Quantification of steroid hormones in hTOr-conditioned medium. Dots: individual samples from two hTSC lines (B31 and CT27; $n = 2$ biological replicates).

(D) hTOr co-cultured with a GFP-expressing hEMO. Scale bars, 200 μm.

(E) hEMO epithelial height in Contact vs. Non-contact regions. Mean ± SD ($n = 5$ regions, 3 experiments). $^{**}p < 0.01$ by linear mixed-effects model.

(F) hEMO lumen retention rate by distance from hTOr. Percentages ± SEP ($n = 1{,}753$ control, 488 Far, 1,134 Mid, 593 near; total 3,968 organoids, 3 experiments). $^{***}p < 0.001$ by Fisher's exact test with Bonferroni correction.

(G) Fused hTOr (KuO, magenta) and hEMO (GFP, cyan). Scale bars, 100 μm.

(H) Fusion efficiency. Volumetric overlap vs. fluorescence mixing for contacting pairs ($n = 35$). Dashed lines: thresholds (>5% overlap, >2-fold mixing). Red dots: fused pairs (68.6%).

(I) Re-clustered UMAP of hEMO cells showing Homeostatic, Cycling, and Activated states.

(J) Marker gene expression on hEMO UMAP.

(K) Oxidative Phosphorylation module scores across hEMO states.

$p < 2.2 \times 10^{-16}$, Kruskal-Wallis test with Wilcoxon rank-sum test, Bonferroni correction.

(L) NicheNet-inferred regulatory potential of hTOr-secreted ligands on co-cultured hEMO.

See also Figure S5.

the receptivity marker *PAEP* (Figure S5F). Crucially, physical interaction frequently culminated in structural fusion, providing a tractable *in vitro* model of histiotrophic support. Immunofluorescence validated the glandular identity of the interacting epithelium, demonstrating that FOXA2^{+} hEMO cells were structurally integrated with hTOr at the contact sites (Figure S5G). 3D image analysis of Kusabira Orange (KuO)-expressing hTOr co-cultured with GFP-hEMO confirmed the efficiency of this process, with 68.6% of contacting pairs exhibiting cytoplasmic fusion based on volumetric overlap and fluorescence mixing (Figures 5G and 5H).

To dissect the molecular basis of this interaction, snRNA-seq revealed a unique 'Activated' hEMO population that emerged specifically upon co-culture (Figures 5I and S5H). Compared with mono-cultured hEMOs, co-cultured hEMO showed reduced WNT-target gene expression while upregulating NOTCH signaling and secretory markers (*PAEP*, *FKBP4*), with *FOXJ1* expression maintained (Figures 5J; S5I and S5J). We refer to the 'Homeostatic' state operationally to denote the relatively low-MKI67, non-activated hEMO population in this *in vitro* system; this nomenclature does not imply functional homeostasis *in vivo*. This transition was characterized by robust upregulation of protein synthesis and cellular energy production programs (Figure S5K); the Activated state exhibited marked increases in oxidative phosphorylation and glycolysis, alongside sustained proliferation ($MKI67^{+}$), exceeding the levels observed in the Homeostatic and Cycling states (Figures 5K and S5L). Integrating our trophoblast secretome data (Figure S5M), NicheNet analysis prioritized hTOr-derived hCG, IGF2, and leptin (LEP) as candidate upstream ligands potentially contributing to this response, linking trophoblast signals to mitochondrial regulation (TSPO) and antioxidant defense (SOD2) in the epithelium (Figure 5L). Thus, hTOr-derived signals promote an endometrial epithelial state distinct from the non-activated baseline state, characterized by enhanced metabolic and secretory programs.

hTOr generate EVT states capable of directional endothelial engagement and vascular remodeling

Beyond endocrine function, successful placentation requires invasive trophoblasts. To determine whether hTOr retain EVT differentiation capacity, we induced differentiation in Matrigel. This generated HLA-G^{+} cells extending from the periphery while preserving the CGB^{+} STB core, a spatial arrangement reminiscent of early invasive trophoblast organization (Figure 6A and S6A–S6C). snRNA-seq reconstructed a continuous trajectory from CTB to terminally differentiated EVT states, marked by the progressive induction of invasion markers (e.g., *HLA-G*, *ITGA5*, *MMP2*) (Figures 6B and 6C). Label transfer to a first-trimester reference atlas[25] supported the emergence of interstitial EVT (iEVT)-like cells, alongside rare populations with transcriptional features associated with endovascular EVT (eEVT) and giant cell (GC) programs (Figures 6D; S6D, and S6E). Consistent with the reference atlas,[25] *FLT4* and *RAC1* were enriched in these putative eEVT (EVT1/2, clusters 1 and 7) and GC (cluster 3) populations, respectively (Figure 6E). Immunofluorescence analysis further identified $FLT4^{+}$ and $RAC1^{+}$ cells within distal organoid-derived EVT outgrowths (Figures 6F and S6F). Functional pathway analysis was consistent with this differentiation trajectory: While proximal progenitors (p/cCTB) exhibited peak proliferation and Notch signaling, differentiation into EVT1-2 was marked by EMT and Interferon signatures. Notably, the GC-associated cluster showed re-engagement of cell-cycle and protein-secretion signatures, reminiscent of programs reported in distal column GCs[47,48] (Figure 6G).

To model vascular interactions, we co-cultured hTOr with HUVECs in a collagen-Matrigel matrix, providing the requisite ECM scaffold for endothelial tube formation (Figure S6G). Strikingly, EVT protrusions exhibited a directional bias toward endothelial structures; migration angles were significantly lower than the 57.3° expected for random 3D orientation (Figures 6H–6J; S6H–S6J). This bias was distance-dependent, reaching a LOESS-smoothed minimum of 48.8° at 18.5 μm and approaching the random baseline at longer distances. Upon contact, EVTs are physically integrated into the vascular network, aligning along vessel tracks (Figures 6K and S6K). Quantitatively, over 60% of contacting EVTs achieved partial or full integration (alignment and elongation) (Figure S6L). Crucially, this interaction was locally destructive, triggering a distance-dependent reduction in endothelial vessel volume at contact sites (Figure 6L). These proximal changes functionally mimic the destructive endothelial remodeling characteristic of maternal spiral artery transformation.

DISCUSSION

This study links physical cues to trophoblast fate and function. Rotational culture is associated with a niche supporting both rapid proliferation—linked to POLQ-mediated genome maintenance—and extensive differentiation driven by a biomechanical balance between reduced YAP activity and peripheral CREB activation, with GCM1 stabilizing trophoblast chromatin state. This coordinated cellular logic enables autonomous endocrine competence and invasive capacity, which we harness to model aspects of the maternal interface and trophoblast-endothelial interaction. While BMP4-based induction of primed hESCs has been proposed to generate trophoblast/primitive syncytium-like states,[49–51] the extent to which these models resolve trophoblast versus amnion identities remains debated.[52–54] Existing Matrigel-embedded and suspension organoid systems remain architecturally limited.[13–15,18–20,55] Our data indicate that matrix-free rotational culture generates polarized hTOr with extensive outer STB domains and promotes dynamic lumenogenesis via fusion of lacuna-like cavities, creating a tractable model for mechanistic and multi-omic analysis.

Transcriptomic mapping[24] indicates that hTOr cells predominantly map to early embryonic/post-implantation (E5–E14) reference profiles rather than first-trimester populations. Stage-specific dynamics emerged: Early populations exhibited MAPK activity, while maturation engaged p53, Hypoxia, and JAK-STAT pathways. We identified POLQ as selectively enriched in early trophoblasts, restricted to S/G2M phases. Although error-prone,[56] POLQ supports rapid expansion; its inhibition induced DSBs in 2D hTSCs and impaired 3D organoid growth while reducing genomic fragmentation. Thus, POLQ likely enables proliferation via timely repair at the cost of genomic scarring,[35] potentially contributing to placental mosaicism.[38]

Architectural differences likely stem from the differential integration of biomechanical cues. In rotational culture, we found selective activation of a CREB1 module, with phospho-CREB enriched at the peripheral STB domain. Although cAMP/PKA signaling is a known fusion driver,[57,58] our findings suggest that hydrodynamic cues are associated with peripheral CREB activation and surface-localized syncytialization.[59] Conversely, Matrigel sustains nuclear YAP activity, maintaining a progenitor state consistent with YAP's established role in CTB stemness.[40,60] Constitutive YAP activation shifts cells to a high-TEAD/low-CREB profile with upregulated mitotic effectors, aligning with a 'cycling differentiation' model where differentiation uncouples from the cell-cycle exit required for terminal syncytialization.

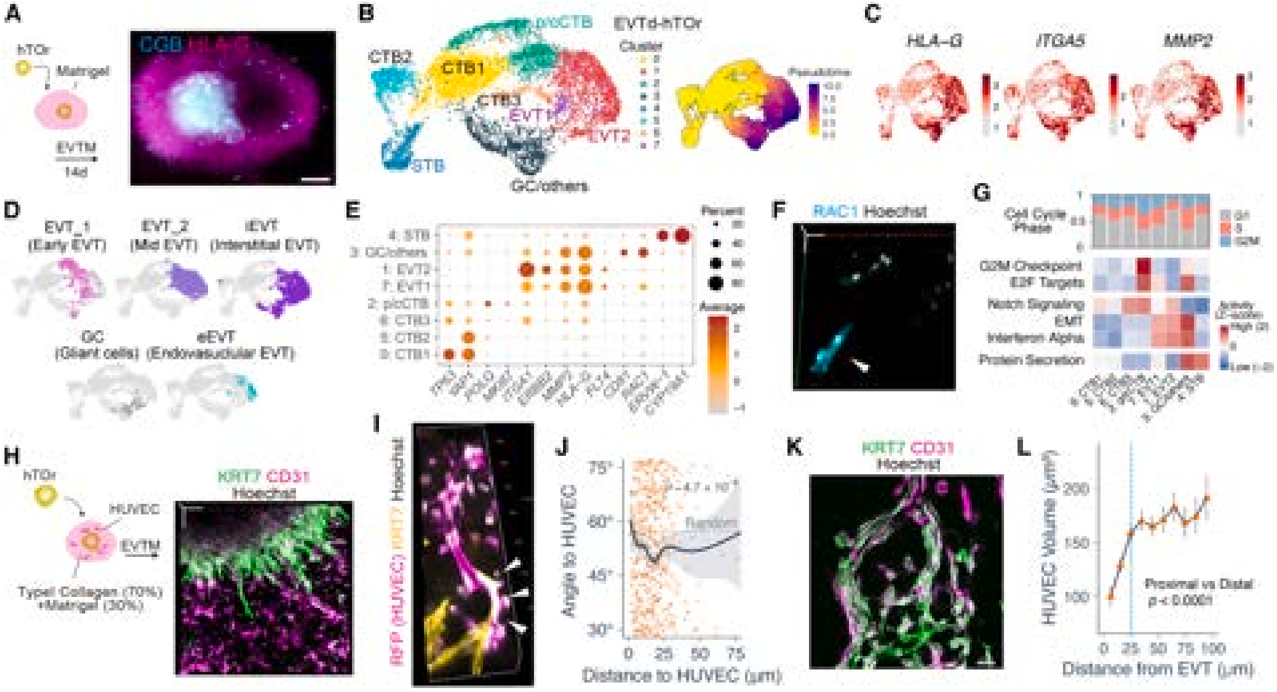

Figure 6. hTOr generates EVT states capable of directional endothelial engagement and vascular remodeling

(A) EVT induction schematic (left) and whole-mount immunofluorescence showing HLA-G$^+$ invasion (magenta) from a CGB$^+$ core (cyan). Scale bars, 500 μm.

(B) UMAP (left) and pseudotime (right) of EVT-differentiated hTOr.

(C) Feature plots of *HLA-G*, *ITGA5*, and *MMP2*.

(D) EVT subtypes (EVT_1, EVT_2, iEVT, eEVT, GC) annotated by label transfer.[25]

(E) Dot plot of representative marker genes across EVT-differentiated clusters. Dot size indicates the percentage of expressing cells; color indicates scaled average expression.

(F) RAC1$^+$ cell (cyan) in EVT-differentiated hTOr. Hoechst, white. 3D reconstruction. Scale indicator, 50 μm.

(G) Cell cycle phase distribution (top) and pathway activity heatmap (bottom) along differentiation trajectory.

(H) hTOr-HUVEC co-culture schematic (left) and 3D reconstruction of KRT7$^+$ trophoblast invasion (green) toward CD31$^+$ endothelial networks (magenta). Scale indicator, 100 μm.

(I) 3D reconstruction of KRT7$^+$ trophoblasts (yellow) associating with RFP$^+$ endothelial cells (magenta). Arrowheads: tubular extensions.

(J) EVT directional bias. Each dot represents one EVT ($n = 921$ from 7 image volumes across 3 independent experiments). Dashed line, random expectation (57.3°); solid line, LOESS fit with 95% confidence interval. Angles were significantly lower than expected (one-sided Wilcoxon signed-rank test, $p = 4.7 \times 10^{-8}$).

(K) KRT7$^+$ trophoblasts (green) integrating into CD31$^+$ networks (magenta). Scale bars, 20 μm.

(L) HUVEC segment volume vs. distance from EVT. Geometric mean ± SEM ($n = 10{,}214$ segments, 7 co-cultures).

$p < 0.0001$ by Wilcoxon rank-sum test for proximal (<25 μm) versus distal (≥25 μm) segments.

See also Figure S6.

Together, these findings support a biomechanical balance model in which rotational culture is associated with peripheral CREB activation and reduced surface YAP activity in matrix-free suspension. By minimizing sedimentation,[61,62] this system likely reduces surface YAP activation while preserving progenitor niches, enabling coexistence of self-renewal and STB maturation. This framework offers a testable hypothesis for regional trophoblast specification *in vivo*,[63] contrasting high-ECM contact areas (e.g., basal plate) with low-contact regions.

Long recognized as a key regulator of STB formation and chorioallantoic branching in mice,[64] GCM1 is also implicated in EVT differentiation.[43,46] In our rotational culture, GCM1 loss blocked STB entry, eliminating lacuna-like lumen formation and fusion dynamics. This phenotype—distinct from the ‘hollow ball’ morphology reported in static suspension[44]—underscores culture-modality dependence. Multiome analysis revealed that GCM1 deficiency destabilizes the progenitor landscape, enabling ‘hijacking’ by KLF/MAZ-family pioneers and ectopic *GATA6* induction. This state, marked by stress-response signatures but lacking canonical primitive endoderm markers, represents a non-canonical lineage destabilization. Together, these findings support a role for GCM1 in stabilizing trophoblast regulatory programs against aberrant chromatin remodeling.

hTOr exhibit steroidogenic and peptide hormone output consistent with trophoblast endocrine competence.[65] Crucially, this endocrine maturation extends to paracrine remodeling of the endometrial epithelium. hTOr-secreted factors, likely including hCG, IGF2, and LEP, induce an endometrial epithelial state marked by transcriptional programs consistent with bioenergetic and secretory activation, distinct from the quiescent decidual state.[66] This state is consistent with the idea that implantation is supported by an active, energy-demanding epithelial response rather than purely passive receptivity.[67,68]

The platform supports a continuous trajectory from cycling progenitors to diverse EVT-associated states. hTOr-derived EVT-associated cells also showed cell-cycle-associated signature reminiscent of programs in distal column GCs.[47,48] Unlike terminal syncytialization, which mandates cell cycle exit, this physiological re-entry highlights the distinct regulatory logic of the EVT lineage. Functionally, hTOr provides a tractable model for selected aspects of trophoblast-vascular interaction, including directional endothelial engagement and destructive remodeling. The observation that EVTs align with and locally remodel endothelial networks—consistent with aspects of spiral artery transformation—establishes a quantitative framework for dissecting invasion mechanisms. Together, these results lay the groundwork for future placental bed models incorporating decidual and immune components.

In summary, our stepwise reconstruction—from biomechanical principles through GCM1-mediated chromatin-state stabilization to maternal and endothelial co-culture—extends current reductionist models by enabling integrated analysis of placental morphogenesis and tissue interactions in a human system.

Limitations of the study

First, endometrial metabolic activation in this study is inferred from transcriptional signatures and awaits direct metabolic validation. Second, the maternal interface modeled here lacks immune components and physiological hemodynamics; vascular remodeling was assessed in a simplified HUVEC/ECM assay rather than in bona fide spiral arteries. Third, developmental-stage assignment relies primarily on transcriptomic projection and therefore does not establish full equivalence to *in vivo* early post-implantation trophoblast states. Fourth, EVT subtype assignments, including rare eEVT- and giant-cell-associated states, are based primarily on transcriptomic signatures and selected marker expression and should therefore be interpreted conservatively. Finally, several mechanistic interpretations, including peripheral CREB activation and trophoblast-derived endometrial signaling, remain inferential and will require direct perturbation.

RESOURCE AVAILABILITY

Lead contact

Further information and requests for resources and reagents should be directed to and will be fulfilled by the lead contact, Shun Shibata (shun.shibata.a3@tohoku.ac.jp).

Materials availability

All unique/stable materials generated in this study are available from the lead contact upon reasonable request with a completed materials transfer agreement.

Data and code availability

- Data: Sequencing data have been deposited in GEO under GSE303893 (hTOr), GSE304580 (hTOr_YAP5SA), GSE305070 (multiome), GSE306469 (EVT differentiation), GSE324114 (hTOr-endometrial co-culture), and GSE324315 (bulk RNA-seq). Low-pass WGS/CNA data have been deposited in SRA under PRJNA1432413 (SRR37482283–SRR37482286; BioSamples SAMN56341663–SAMN56341666). The mass spectrometry proteomics data have been deposited to the ProteomeXchange Consortium via the PRIDE partner repository with the dataset identifier PXD075393. All accession codes are also listed in the key resources table.
- Code: This paper does not report original custom code or new algorithms. Analyses were performed using publicly available software packages and standard workflows described in the STAR Methods.
- Other items: Any additional information required to reanalyze the data reported in this paper is available from the lead contact upon request.

ACKNOWLEDGMENTS

We thank Fredrik Lanner, Cheng Zhao, and Sophie Petropoulos (Karolinska Institutet) for sharing analysis scripts and reference datasets for projection to the extended human embryonic atlas; N. Miyauchi and E. Shoji for administrative support; and the Biomedical Research Core of Tohoku University Graduate School of Medicine for facility support. This work was supported by JSPS KAKENHI (24H01389 and 24K18122), the Uehara Memorial Foundation, the Naito Foundation, the Mitsubishi Foundation, the Takeda Science Foundation, the Mochida Memorial Foundation, the Smoking Research Foundation, and the JST FOREST Program (JPMJFR244O) (all to S.S.).

AUTHOR CONTRIBUTIONS

S.S. conceived the study, performed experiments, analyzed data, wrote the manuscript, and prepared the figures. Y.I. and M.K. performed experiments and analyzed data. H.O. provided CRISPR-mediated KO cell lines and supervised stem cell and organoid culture conditions. T.A. secured funding and established the research environment.

DECLARATION OF INTERESTS

T.A. serves as Chief Scientific Officer and board member of TSC Co., Ltd. This affiliation is disclosed for transparency and has no direct influence on the study design, data analysis, or interpretation of the results. All other authors declare no competing interests.

DECLARATION OF GENERATIVE AI AND AI-ASSISTED TECHNOLOGIES IN THE WRITING PROCESS

During the preparation of this work, the authors used ChatGPT (OpenAI) and Gemini (Google) to improve language clarity and troubleshoot analysis code. The authors reviewed and edited the content as needed and take full responsibility for the content of the publication.

STAR★METHODS

Detailed methods are provided in the online version of this paper and include the following:

- KEY RESOURCES TABLE
- EXPERIMENTAL MODEL AND STUDY PARTICIPANT DETAILS
  - Ethics statement and human tissue-derived organoids
  - Sex as a biological variable
  - Human trophoblast stem cell lines and derived trophoblast organoids
  - Human endometrial organoids
  - HUVECs and 293 T cells
- METHOD DETAILS
  - hTSC culture
  - Spheroid formation assay (factor drop-out)
  - Generation of hTSC spheroids and rotation-cultured human trophoblast organoids (hTOr)
  - Immunofluorescence staining and imaging
  - Quantification of syncytiotrophoblast surface coverage
  - Permeability barrier assay
  - Quantification of apoptosis

  - ○ Transmission electron microscopy (TEM)
  - ○ Organoid passaging
  - ○ snRNA-seq and analysis
  - ○ Cell cycle analysis
  - ○ Normalization and integration
  - ○ Dimensionality reduction and clustering
  - ○ Label transfer and cell type prediction
  - ○ RNA velocity and pseudotime analysis
  - ○ Projection onto the extended human embryonic reference
  - ○ Maturation score and gene correlation
  - ○ Inference of transcription factor and pathway activities
  - ○ Force-directed network topology analysis
  - ○ Target prioritization and waterfall visualization
  - ○ Functional enrichment and semantic clustering
  - ○ Phase-space trajectory analysis
  - ○ Functional module scoring and trajectory analysis
  - ○ Statistical analysis and enrichment
  - ○ In situ gelatinase activity assay
  - ○ γH2AX-focus formation and nuclear morphology assay
  - ○ Low-pass whole genome sequencing (WGS) and CNA analysis
  - ○ Bulk RNA-seq and analysis
  - ○ Gene set enrichment analysis (GSEA)
  - ○ Inference of transcription factor activity and GRN construction
  - ○ Quantification of spatial fluorescence distribution
  - ○ Generation of doxycycline-inducible YAP5SA hTSC line
  - ○ 2D monolayer culture and serial passaging analysis
  - ○ Structural modeling and visualization
  - ○ Single-cell multiome analysis
  - ○ Normalization and multimodal integration
  - ○ Pseudotime trajectory analysis
  - ○ TF target module analysis
  - ○ Differential gene expression analysis
  - ○ Chromatin accessibility and motif analysis
  - ○ Cell cycle scoring (multiome)
  - ○ Integrated motif analysis and biophysical deconvolution
  - ○ Reconstruction of gene regulatory networks
  - ○ Peak-gene linkage and regulatory analysis
  - ○ Integration of motif accessibility and gene expression
  - ○ Primitive endoderm marker analysis
  - ○ Acquisition of hTOr-conditioned medium (hTOr-CM)
  - ○ LC-MS/MS
  - ○ Proteomic analysis
  - ○ Quantification of human chorionic gonadotropin (hCG)
  - ○ 3D Co-culture assays
  - ○ Quantification of epithelial height
  - ○ Automated morphometric analysis of Co-cultures
  - ○ Quantification of organoid fusion
  - ○ Single-nucleus RNA-seq analysis of Co-culture system
- QUANTIFICATION AND STATISTICAL ANALYSIS

SUPPLEMENTAL INFORMATION

Supplementary data related to this article can be found online at https://doi.org/10.1016/j.celrep.2026.117637.

Received: August 15, 2025
Revised: May 15, 2026
Accepted: June 12, 2026

REFERENCES

1. Burton, G.J., and Fowden, A.L. (2015). The placenta: a multifaceted, transient organ. Philos. Trans. R. Soc. Lond. B Biol. Sci. *370*, 20140066. https://doi.org/10.1098/rstb.2014.0066.
2. Maltepe, E., and Fisher, S.J. (2015). Placenta: the forgotten organ. Annu. Rev. Cell Dev. Biol. *31*, 523–552. https://doi.org/10.1146/annurev-cellbio-100814-125620.
3. Shibata, S., Kobayashi, E.H., Kobayashi, N., Oike, A., Okae, H., and Arima, T. (2020). Unique features and emerging in vitro models of human placental development. Reprod. Med. Biol. *19*, 301–313. https://doi.org/10.1002/rmb2.12347.
4. Norwitz, E.R., Schust, D.J., and Fisher, S.J. (2001). Implantation and the survival of early pregnancy. N. Engl. J. Med. *345*, 1400–1408. https://doi.org/10.1056/NEJMra000763.
5. Burton, G.J., Jauniaux, E., and Charnock-Jones, D.S. (2010). The influence of the intrauterine environment on human placental development. Int. J. Dev. Biol. *54*, 303–312. https://doi.org/10.1387/ijdb.082764gb.
6. Knöfler, M., and Pollheimer, J. (2013). Human placental trophoblast invasion and differentiation: a particular focus on Wnt signaling. Front. Genet. *4*, 190. https://doi.org/10.3389/fgene.2013.00190.
7. Huppertz, B. (2008). The anatomy of the normal placenta. J. Clin. Pathol. *61*, 1296–1302. https://doi.org/10.1136/jcp.2008.055277.
8. Castellucci, M., Kosanke, G., Verdenelli, F., Huppertz, B., and Kaufmann, P. (2000). Villous sprouting: fundamental mechanisms of human placental development. Hum. Reprod. Update *6*, 485–494. https://doi.org/10.1093/humupd/6.5.485.
9. Deglincerti, A., Croft, G.F., Pietila, L.N., Zernicka-Goetz, M., Siggia, E.D., and Brivanlou, A.H. (2016). Self-organization of the in vitro attached human embryo. Nature *533*, 251–254. https://doi.org/10.1038/nature17948.
10. Shahbazi, M.N., Jedrusik, A., Vuoristo, S., Recher, G., Hupalowska, A., Bolton, V., Fogarty, N.M.E., Campbell, A., Devito, L.G., Ilic, D., et al. (2016). Self-organization of the human embryo in the absence of maternal tissues. Nat. Cell Biol. *18*, 700–708. https://doi.org/10.1038/ncb3347.
11. Xiang, L., Yin, Y., Zheng, Y., Ma, Y., Li, Y., Zhao, Z., Guo, J., Ai, Z., Niu, Y., Duan, K., et al. (2020). A developmental landscape of 3D-cultured human pre-gastrulation embryos. Nature *577*, 537–542. https://doi.org/10.1038/s41586-019-1875-y.
12. Okae, H., Toh, H., Sato, T., Hiura, H., Takahashi, S., Shirane, K., Kabayama, Y., Suyama, M., Sasaki, H., and Arima, T. (2018). Derivation of Human Trophoblast Stem Cells. Cell Stem Cell *22*, 50–63.e6. https://doi.org/10.1016/j.stem.2017.11.004.
13. Haider, S., Meinhardt, G., Saleh, L., Kunihs, V., Gamperl, M., Kaindl, U., Ellinger, A., Burkard, T.R., Fiala, C., Pollheimer, J., et al. (2018). Self-Renewing Trophoblast Organoids Recapitulate the Developmental Program of the Early Human Placenta. Stem Cell Rep. *11*, 537–551. https://doi.org/10.1016/j.stemcr.2018.07.004.
14. Turco, M.Y., Gardner, L., Kay, R.G., Hamilton, R.S., Prater, M., Hollinshead, M.S., McWhinnie, A., Esposito, L., Fernando, R., Skelton, H., et al. (2018). Trophoblast organoids as a model for maternal-fetal interactions during human placentation. Nature *564*, 263–267. https://doi.org/10.1038/s41586-018-0753-3.
15. Karvas, R.M., Khan, S.A., Verma, S., Yin, Y., Kulkarni, D., Dong, C., Park, K.M., Chew, B., Sane, E., Fischer, L.A., et al. (2022). Stem-cell-derived trophoblast organoids model human placental development and susceptibility to emerging pathogens. Cell Stem Cell *29*, 810–825.e8. https://doi.org/10.1016/j.stem.2022.04.004.
16. Sheridan, M.A., Zhao, X., Fernando, R.C., Gardner, L., Perez-Garcia, V., Li, Q., Marsh, S.G.E., Hamilton, R., Moffett, A., and Turco, M.Y. (2021). Characterization of primary models of human trophoblast. Development *148*, dev199749. https://doi.org/10.1242/dev.199749.
17. Shannon, M.J., McNeill, G.L., Koksal, B., Baltayeva, J., Wächter, J., Castellana, B., Peñaherrera, M.S., Robinson, W.P., Leung, P.C.K., and Beristain, A.G. (2024). Single-cell assessment of primary and stem cell-derived human trophoblast organoids as placenta-modeling platforms. Dev. Cell *59*, 776–792.e11. https://doi.org/10.1016/j.devcel.2024.01.023.
18. Hori, T., Okae, H., Shibata, S., Kobayashi, N., Kobayashi, E.H., Oike, A., Sekiya, A., Arima, T., and Kaji, H. (2024). Trophoblast stem cell-based

organoid models of the human placental barrier. Nat. Commun. *15*, 962. https://doi.org/10.1038/s41467-024-45279-y.

19. Yang, L., Liang, P., Yang, H., and Coyne, C.B. (2024). Trophoblast organoids with physiological polarity model placental structure and function. J. Cell Sci. *137*, jcs261528. https://doi.org/10.1242/jcs.261528.
20. Zhou, J., Sheridan, M.A., Tian, Y., Dahlgren, K.J., Messler, M., Peng, T., Zhao, A., Ezashi, T., Schulz, L.C., Ulery, B.D., et al. (2025). Development of apical out trophoblast stem cell derived organoids to model early human pregnancy. iScience *28*, 112099. https://doi.org/10.1016/j.isci.2025.112099.
21. Shibata, S., Endo, S., Nagai, L.A.E., H Kobayashi, E., Oike, A., Kobayashi, N., Kitamura, A., Hori, T., Nashimoto, Y., Nakato, R., et al. (2024). Modeling embryo-endometrial interface recapitulating human embryo implantation. Sci. Adv. *10*, eadi4819. https://doi.org/10.1126/sciadv.adi4819.
22. O'Rahilly, R., and Müller, F. (1987). Developmental Stages in Human Embryos : Including a Revision of Streeter's "Horizons" and a Survey of the Carnegie Collection (Carnegie Institution of Washington).
23. Hertig, A.T., Rock, J., and Adams, E.C. (1956). A description of 34 human ova within the first 17 days of development. Am. J. Anat. *98*, 435–493. https://doi.org/10.1002/aja.1000980306.
24. Zhao, C., Plaza Reyes, A., Schell, J.P., Weltner, J., Ortega, N.M., Zheng, Y., Björklund, Å.K., Baqué-Vidal, L., Sokka, J., Trokovic, R., et al. (2025). A comprehensive human embryo reference tool using single-cell RNA-sequencing data. Nat. Methods *22*, 193–206. https://doi.org/10.1038/s41592-024-02493-2.
25. Arutyunyan, A., Roberts, K., Troulé, K., Wong, F.C.K., Sheridan, M.A., Kats, I., Garcia-Alonso, L., Velten, B., Hoo, R., Ruiz-Morales, E.R., et al. (2023). Spatial multiomics map of trophoblast development in early pregnancy. Nature *616*, 143–151. https://doi.org/10.1038/s41586-023-05869-0.
26. Baczyk, D., Drewlo, S., Proctor, L., Dunk, C., Lye, S., and Kingdom, J. (2009). Glial cell missing-1 transcription factor is required for the differentiation of the human trophoblast. Cell Death Differ. *16*, 719–727. https://doi.org/10.1038/cdd.2009.1.
27. Majali-Martinez, A., Hiden, U., Ghaffari-Tabrizi-Wizsy, N., Lang, U., Desoye, G., and Dieber-Rotheneder, M. (2016). Placental membrane-type metalloproteinases (MT-MMPs): Key players in pregnancy. Cell Adh. Migr. *10*, 136–146. https://doi.org/10.1080/19336918.2015.1110671.
28. Ahmad, S., and Ahmed, A. (2004). Elevated placental soluble vascular endothelial growth factor receptor-1 inhibits angiogenesis in preeclampsia. Circ. Res. *95*, 884–891. https://doi.org/10.1161/01.RES.0000147365.86159.f5.
29. Yoshie, M., Ohishi, K., Ishikawa, G., Tsuru, A., Kusama, K., Azumi, M., and Tamura, K. (2023). Small GTP-binding protein Rap1 mediates EGF and HB-EGF signaling and modulates EGF receptor expression in HTR-8/SVneo extravillous trophoblast cells. Reprod. Med. Biol. *22*, e12537. https://doi.org/10.1002/rmb2.12537.
30. Gonzalez, I.M., Ackerman, W.E., 4th, Vandre, D.D., and Robinson, J.M. (2014). Exocyst complex protein expression in the human placenta. Placenta *35*, 442–449. https://doi.org/10.1016/j.placenta.2014.04.015.
31. Gauster, M., Maninger, S., Siwetz, M., Deutsch, A., El-Heliebi, A., Kolb-Lenz, D., Hiden, U., Desoye, G., Herse, F., and Prokesch, A. (2018). Downregulation of p53 drives autophagy during human trophoblast differentiation. Cell. Mol. Life Sci. *75*, 1839–1855. https://doi.org/10.1007/s00018-017-2695-6.
32. Bayer, A., Lennemann, N.J., Ouyang, Y., Bramley, J.C., Morosky, S., Marques, E., Jr, Cherry, S., Sadovsky, Y., and Coyne, C.B. (2016). Type III Interferons Produced by Human Placental Trophoblasts Confer Protection against Zika Virus Infection. Cell Host Microbe *19*, 705–712. https://doi.org/10.1016/j.chom.2016.03.008.
33. Caniggia, I., and Winter, J.L. (2002). Adriana and Luisa Castellucci Award lecture 2001. Hypoxia inducible factor-1: oxygen regulation of trophoblast differentiation in normal and pre-eclamptic pregnancies–a review. Placenta *23*, S47–S57. https://doi.org/10.1053/plac.2002.0815.
34. Daoud, G., Amyot, M., Rassart, E., Masse, A., Simoneau, L., and Lafond, J. (2005). ERK1/2 and p38 regulate trophoblasts differentiation in human term placenta. J. Physiol. *566*, 409–423. https://doi.org/10.1113/jphysiol.2005.089326.
35. Ramsden, D.A., Carvajal-Garcia, J., and Gupta, G.P. (2022). Mechanism, cellular functions and cancer roles of polymerase-theta-mediated DNA end joining. Nat. Rev. Mol. Cell Biol. *23*, 125–140. https://doi.org/10.1038/s41580-021-00405-2.
36. Vento-Tormo, R., Efremova, M., Botting, R.A., Turco, M.Y., Vento-Tormo, M., Meyer, K.B., Park, J.E., Stephenson, E., Polański, K., Goncalves, A., et al. (2018). Single-cell reconstruction of the early maternal-fetal interface in humans. Nature *563*, 347–353. https://doi.org/10.1038/s41586-018-0698-6.
37. Zhou, J., Gelot, C., Pantelidou, C., Li, A., Yücel, H., Davis, R.E., Färkkilä, A., Kochupurakkal, B., Syed, A., Shapiro, G.I., et al. (2021). A first-in-class Polymerase Theta Inhibitor selectively targets Homologous-Recombination-Deficient Tumors. Nat. Cancer *2*, 598–610. https://doi.org/10.1038/s43018-021-00203-x.
38. Coorens, T.H.H., Oliver, T.R.W., Sanghvi, R., Sovio, U., Cook, E., Vento-Tormo, R., Haniffa, M., Young, M.D., Rahbari, R., Sebire, N., et al. (2021). Inherent mosaicism and extensive mutation of human placentas. Nature *592*, 80–85. https://doi.org/10.1038/s41586-021-03345-1.
39. Zanconato, F., Forcato, M., Battilana, G., Azzolin, L., Quaranta, E., Bodega, B., Rosato, A., Bicciato, S., Cordenonsi, M., and Piccolo, S. (2015). Genome-wide association between YAP/TAZ/TEAD and AP-1 at enhancers drives oncogenic growth. Nat. Cell Biol. *17*, 1218–1227. https://doi.org/10.1038/ncb3216.
40. Meinhardt, G., Haider, S., Kunihs, V., Saleh, L., Pollheimer, J., Fiala, C., Hetey, S., Feher, Z., Szilagyi, A., Than, N.G., and Knöfler, M. (2020). Pivotal role of the transcriptional co-activator YAP in trophoblast stemness of the developing human placenta. Proc. Natl. Acad. Sci. USA *117*, 13562–13570. https://doi.org/10.1073/pnas.2002630117.
41. Dupont, S., Morsut, L., Aragona, M., Enzo, E., Giulitti, S., Cordenonsi, M., Zanconato, F., Le Digabel, J., Forcato, M., Bicciato, S., et al. (2011). Role of YAP/TAZ in mechanotransduction. Nature *474*, 179–183. https://doi.org/10.1038/nature10137.
42. Dasgupta, I., and McCollum, D. (2019). Control of cellular responses to mechanical cues through YAP/TAZ regulation. J. Biol. Chem. *294*, 17693–17706. https://doi.org/10.1074/jbc.REV119.007963.
43. Shimizu, T., Oike, A., Kobayashi, E.H., Sekiya, A., Kobayashi, N., Shibata, S., Hamada, H., Saito, M., Yaegashi, N., Suyama, M., et al. (2023). CRISPR screening in human trophoblast stem cells reveals both shared and distinct aspects of human and mouse placental development. Proc. Natl. Acad. Sci. USA *120*, e2311372120. https://doi.org/10.1073/pnas.2311372120.
44. Cinkornpumin, J.K., Kwon, S.Y., Prandstetter, A.M., Maxian, T., Sirois, J., Goldberg, J., Zhang, J., Saini, D., Dasgupta, P., Jeyarajah, M.J., et al. (2025). Hypoxia and loss of GCM1 expression prevent differentiation and contact inhibition in human trophoblast stem cells. Stem Cell Rep. *20*, 102481. https://doi.org/10.1016/j.stemcr.2025.102481.
45. Cohen, S.X., Moulin, M., Hashemolhosseini, S., Kilian, K., Wegner, M., and Müller, C.W. (2003). Structure of the GCM domain-DNA complex: a DNA-binding domain with a novel fold and mode of target site recognition. EMBO J. *22*, 1835–1845. https://doi.org/10.1093/emboj/cdg182.
46. Jeyarajah, M.J., Jaju Bhattad, G., Kelly, R.D., Baines, K.J., Jaremek, A., Yang, F.H.P., Okae, H., Arima, T., Dumeaux, V., and Renaud, S.J. (2022). The multifaceted role of GCM1 during trophoblast differentiation in the human placenta. Proc. Natl. Acad. Sci. USA *119*, e2203071119. https://doi.org/10.1073/pnas.2203071119.
47. Zybina, T.G., Kaufmann, P., Frank, H.G., Freed, J., Kadyrov, M., and Biesterfeld, S. (2002). Genome multiplication of extravillous trophoblast cells in human placenta in the course of differentiation and invasion

into endometrium and myometrium. I. Dynamics of polyploidization. Tsitologiia *44*, 1058–1067.

48. Morey, R., Farah, O., Kallol, S., Requena, D.F., Meads, M., Moretto-Zita, M., Soncin, F., Laurent, L.C., and Parast, M.M. (2021). Transcriptomic Drivers of Differentiation, Maturation, and Polyploidy in Human Extravillous Trophoblast. Front. Cell Dev. Biol. *9*, 702046. https://doi.org/10.3389/fcell.2021.702046.

49. Amita, M., Adachi, K., Alexenko, A.P., Sinha, S., Schust, D.J., Schulz, L.C., Roberts, R.M., and Ezashi, T. (2013). Complete and unidirectional conversion of human embryonic stem cells to trophoblast by BMP4. Proc. Natl. Acad. Sci. USA *110*, E1212–E1221. https://doi.org/10.1073/pnas.1303094110.

50. Yabe, S., Alexenko, A.P., Amita, M., Yang, Y., Schust, D.J., Sadovsky, Y., Ezashi, T., and Roberts, R.M. (2016). Comparison of syncytiotrophoblast generated from human embryonic stem cells and from term placentas. Proc. Natl. Acad. Sci. USA *113*, E2598–E2607. https://doi.org/10.1073/pnas.1601630113.

51. Xu, R.H., Chen, X., Li, D.S., Li, R., Addicks, G.C., Glennon, C., Zwaka, T.P., and Thomson, J.A. (2002). BMP4 initiates human embryonic stem cell differentiation to trophoblast. Nat. Biotechnol. *20*, 1261–1264. https://doi.org/10.1038/nbt761.

52. Guo, G., Stirparo, G.G., Strawbridge, S.E., Spindlow, D., Yang, J., Clarke, J., Dattani, A., Yanagida, A., Li, M.A., Myers, S., et al. (2021). Human naive epiblast cells possess unrestricted lineage potential. Cell Stem Cell *28*, 1040–1056.e6. https://doi.org/10.1016/j.stem.2021.02.025.

53. Io, S., Kabata, M., Iemura, Y., Semi, K., Morone, N., Minagawa, A., Wang, B., Okamoto, I., Nakamura, T., Kojima, Y., et al. (2021). Capturing human trophoblast development with naive pluripotent stem cells in vitro. Cell Stem Cell *28*, 1023–1039.e13. https://doi.org/10.1016/j.stem.2021.03.013.

54. Seetharam, A.S., Vu, H.T.H., Choi, S., Khan, T., Sheridan, M.A., Ezashi, T., Roberts, R.M., and Tuteja, G. (2022). The product of BMP-directed differentiation protocols for human primed pluripotent stem cells is placental trophoblast and not amnion. Stem Cell Rep. *17*, 1289–1302. https://doi.org/10.1016/j.stemcr.2022.04.014.

55. Keenen, M.M., Yang, L., Liang, H., Farmer, V.J., Worota, R.E., Singh, R., Gladfelter, A.S., and Coyne, C.B. (2025). Comparative analysis of the syncytiotrophoblast in placenta tissue and trophoblast organoids using snRNA sequencing. eLife *13*, RP101170. https://doi.org/10.7554/eLife.101170.3.

56. Carvajal-Garcia, J., Cho, J.E., Carvajal-Garcia, P., Feng, W., Wood, R.D., Sekelsky, J., Gupta, G.P., Roberts, S.A., and Ramsden, D.A. (2020). Mechanistic basis for microhomology identification and genome scarring by polymerase theta. Proc. Natl. Acad. Sci. USA *117*, 8476–8485. https://doi.org/10.1073/pnas.1921791117.

57. Zhou, Z., Wang, R., Yang, X., Lu, X.Y., Zhang, Q., Wang, Y.L., Wang, H., Zhu, C., Lin, H.Y., and Wang, H. (2014). The cAMP-responsive element binding protein (CREB) transcription factor regulates furin expression during human trophoblast syncytialization. Placenta *35*, 907–918. https://doi.org/10.1016/j.placenta.2014.07.017.

58. Toufaily, C., Lokossou, A.G., Vargas, A., Rassart, É., and Barbeau, B. (2015). A CRE/AP-1-like motif is essential for induced syncytin-2 expression and fusion in human trophoblast-like model. PLoS One *10*, e0121468. https://doi.org/10.1371/journal.pone.0121468.

59. Kim, P.G., Nakano, H., Das, P.P., Chen, M.J., Rowe, R.G., Chou, S.S., Ross, S.J., Sakamoto, K.M., Zon, L.I., Schlaeger, T.M., et al. (2015). Flow-induced protein kinase A-CREB pathway acts via BMP signaling to promote HSC emergence. J. Exp. Med. *212*, 633–648. https://doi.org/10.1084/jem.20141514.

60. Mizutani, T., Orisaka, M., Miyazaki, Y., Morichika, R., Uesaka, M., Miyamoto, K., and Yoshida, Y. (2022). Inhibition of YAP/TAZ-TEAD activity induces cytotrophoblast differentiation into syncytiotrophoblast in human trophoblast. Mol. Hum. Reprod. *28*, gaac032. https://doi.org/10.1093/molehr/gaac032.

61. Grimm, D., Egli, M., Krüger, M., Riwaldt, S., Corydon, T.J., Kopp, S., Wehland, M., Wise, P., Infanger, M., Mann, V., and Sundaresan, A. (2018). Tissue Engineering Under Microgravity Conditions-Use of Stem Cells and Specialized Cells. Stem Cell. Dev. *27*, 787–804. https://doi.org/10.1089/scd.2017.0242.

62. Imura, T., Otsuka, T., Kawahara, Y., and Yuge, L. (2019). "Microgravity" as a unique and useful stem cell culture environment for cell-based therapy. Regen. Ther. *12*, 2–5. https://doi.org/10.1016/j.reth.2019.03.001.

63. Inohaya, A., Chigusa, Y., Takakura, M., Io, S., Kim, M.A., Matsuzaka, Y., Yasuda, E., Ueda, Y., Kawamura, Y., Takamatsu, S., et al. (2024). Shear stress in the intervillous space promotes syncytial formation of iPS cells-derived trophoblastsdagger. Biol. Reprod. *110*, 300–309. https://doi.org/10.1093/biolre/ioad143.

64. Anson-Cartwright, L., Dawson, K., Holmyard, D., Fisher, S.J., Lazzarini, R.A., and Cross, J.C. (2000). The glial cells missing-1 protein is essential for branching morphogenesis in the chorioallantoic placenta. Nat. Genet. *25*, 311–314. https://doi.org/10.1038/77076.

65. Tuckey, R.C. (2005). Progesterone synthesis by the human placenta. Placenta *26*, 273–281. https://doi.org/10.1016/j.placenta.2004.06.012.

66. Garcia-Alonso, L., Handfield, L.F., Roberts, K., Nikolakopoulou, K., Fernando, R.C., Gardner, L., Woodhams, B., Arutyunyan, A., Polanski, K., Hoo, R., et al. (2021). Mapping the temporal and spatial dynamics of the human endometrium in vivo and in vitro. Nat. Genet. *53*, 1698–1711. https://doi.org/10.1038/s41588-021-00972-2.

67. Chen, Z., and Dean, M. (2023). Endometrial Glucose Metabolism During Early Pregnancy. Reprod. Fertil. *4*, e230016. https://doi.org/10.1530/RAF-23-0016.

68. Zhang, L.X., Song, J.W., Ma, Y.D., Wang, Y.C., Cui, Z.H., Long, Y., Yuan, D.Z., Zhang, J.H., Hu, Y., Yu, L.L., et al. (2021). Expression of SGLT1 in the Mouse Endometrial Epithelium and its Role in Early Embryonic Development and Implantation. Reprod. Sci. *28*, 3094–3108. https://doi.org/10.1007/s43032-021-00480-y.

69. Zhao, B., Wei, X., Li, W., Udan, R.S., Yang, Q., Kim, J., Xie, J., Ikenoue, T., Yu, J., Li, L., et al. (2007). Inactivation of YAP oncoprotein by the Hippo pathway is involved in cell contact inhibition and tissue growth control. Genes Dev. *21*, 2747–2761. https://doi.org/10.1101/gad.1602907.

70. Takahashi, S., Okae, H., Kobayashi, N., Kitamura, A., Kumada, K., Yaegashi, N., and Arima, T. (2019). Loss of p57(KIP2) expression confers resistance to contact inhibition in human androgenetic trophoblast stem cells. Proc. Natl. Acad. Sci. USA *116*, 26606–26613. https://doi.org/10.1073/pnas.1916019116.

71. Hao, Y., Hao, S., Andersen-Nissen, E., Mauck, W.M., 3rd, Zheng, S., Butler, A., Lee, M.J., Wilk, A.J., Darby, C., Zager, M., et al. (2021). Integrated analysis of multimodal single-cell data. Cell *184*, 3573–3587.e29. https://doi.org/10.1016/j.cell.2021.04.048.

72. Stuart, T., Srivastava, A., Madad, S., Lareau, C.A., and Satija, R. (2021). Single-cell chromatin state analysis with Signac. Nat. Methods *18*, 1333–1341. https://doi.org/10.1038/s41592-021-01282-5.

73. Bergen, V., Lange, M., Peidli, S., Wolf, F.A., and Theis, F.J. (2020). Generalizing RNA velocity to transient cell states through dynamical modeling. Nat. Biotechnol. *38*, 1408–1414. https://doi.org/10.1038/s41587-020-0591-3.

74. La Manno, G., Soldatov, R., Zeisel, A., Braun, E., Hochgerner, H., Petukhov, V., Lidschreiber, K., Kastriti, M.E., Lönnerberg, P., Furlan, A., et al. (2018). RNA velocity of single cells. Nature *560*, 494–498. https://doi.org/10.1038/s41586-018-0414-6.

75. Cao, J., Spielmann, M., Qiu, X., Huang, X., Ibrahim, D.M., Hill, A.J., Zhang, F., Mundlos, S., Christiansen, L., Steemers, F.J., et al. (2019). The single-cell transcriptional landscape of mammalian organogenesis. Nature *566*, 496–502. https://doi.org/10.1038/s41586-019-0969-x.

76. Yu, G., Wang, L.G., Han, Y., and He, Q.Y. (2012). clusterProfiler: an R package for comparing biological themes among gene clusters. OMICS A J. Integr. Biol. *16*, 284–287. https://doi.org/10.1089/omi.2011.0118.

77. Vasimuddin, M., Misra, S., Li, H., and Aluru, S. (2019). Efficient Architecture-Aware Acceleration of BWA-MEM for Multicore Systems. Int Parall Distrib *P*, 314–324. https://doi.org/10.1109/Ipdps.2019.00041.
78. Li, H., Handsaker, B., Wysoker, A., Fennell, T., Ruan, J., Homer, N., Marth, G., Abecasis, G., Durbin, R., and Proc, G.P.D. (2009). The Sequence Alignment/Map format and SAMtools. Bioinformatics *25*, 2078–2079. https://doi.org/10.1093/bioinformatics/btp352.
79. Scheinin, I., Sie, D., Bengtsson, H., van de Wiel, M.A., Olshen, A.B., van Thuijl, H.F., van Essen, H.F., Eijk, P.P., Rustenburg, F., Meijer, G.A., et al. (2014). DNA copy number analysis of fresh and formalin-fixed specimens by shallow whole-genome sequencing with identification and exclusion of problematic regions in the genome assembly. Genome Res. *24*, 2022–2032. https://doi.org/10.1101/gr.175141.114.
80. Dobin, A., Davis, C.A., Schlesinger, F., Drenkow, J., Zaleski, C., Jha, S., Batut, P., Chaisson, M., and Gingeras, T.R. (2013). STAR: ultrafast universal RNA-seq aligner. Bioinformatics *29*, 15–21. https://doi.org/10.1093/bioinformatics/bts635.
81. Li, B., and Dewey, C.N. (2011). RSEM: accurate transcript quantification from RNA-Seq data with or without a reference genome. BMC Bioinf. *12*, 323. https://doi.org/10.1186/1471-2105-12-323.
82. Schep, A.N., Wu, B., Buenrostro, J.D., and Greenleaf, W.J. (2017). chromVAR: inferring transcription-factor-associated accessibility from single-cell epigenomic data. Nat. Methods *14*, 975–978. https://doi.org/10.1038/nmeth.4401.
83. Street, K., Risso, D., Fletcher, R.B., Das, D., Ngai, J., Yosef, N., Purdom, E., and Dudoit, S. (2018). Slingshot: cell lineage and pseudotime inference for single-cell transcriptomics. BMC Genom. *19*, 477. https://doi.org/10.1186/s12864-018-4772-0.
84. Zheng, S.C., Stein-O'Brien, G., Augustin, J.J., Slosberg, J., Carosso, G.A., Winer, B., Shin, G., Bjornsson, H.T., Goff, L.A., and Hansen, K.D. (2022). Universal prediction of cell-cycle position using transfer learning. Genome Biol. *23*, 41. https://doi.org/10.1186/s13059-021-02581-y.
85. Love, M.I., Huber, W., and Anders, S. (2014). Moderated estimation of fold change and dispersion for RNA-seq data with DESeq2. Genome Biol. *15*, 550. https://doi.org/10.1186/s13059-014-0550-8.
86. Schneider, C.A., Rasband, W.S., and Eliceiri, K.W. (2012). NIH Image to ImageJ: 25 years of image analysis. Nat. Methods *9*, 671–675. https://doi.org/10.1038/nmeth.2089.
87. Alvarez, M.J., Shen, Y., Giorgi, F.M., Lachmann, A., Ding, B.B., Ye, B.H., and Califano, A. (2016). Functional characterization of somatic mutations in cancer using network-based inference of protein activity. Nat. Genet. *48*, 838–847. https://doi.org/10.1038/ng.3593.
88. Garcia-Alonso, L., Holland, C.H., Ibrahim, M.M., Turei, D., and Saez-Rodriguez, J. (2019). Benchmark and integration of resources for the estimation of human transcription factor activities. Genome Res. *29*, 1363–1375. https://doi.org/10.1101/gr.240663.118.
89. Schubert, M., Klinger, B., Klünemann, M., Sieber, A., Uhlitz, F., Sauer, S., Garnett, M.J., Blüthgen, N., and Saez-Rodriguez, J. (2018). Perturbation-response genes reveal signaling footprints in cancer gene expression. Nat. Commun. *9*, 20. https://doi.org/10.1038/s41467-017-02391-6.
90. Stringer, C., Wang, T., Michaelos, M., and Pachitariu, M. (2021). Cellpose: a generalist algorithm for cellular segmentation. Nat. Methods *18*, 100–106. https://doi.org/10.1038/s41592-020-01018-x.
91. Demichev, V., Messner, C.B., Vernardis, S.I., Lilley, K.S., and Ralser, M. (2020). DIA-NN: neural networks and interference correction enable deep proteome coverage in high throughput. Nat. Methods *17*, 41–44. https://doi.org/10.1038/s41592-019-0638-x.
92. Browaeys, R., Saelens, W., and Saeys, Y. (2020). NicheNet: modeling intercellular communication by linking ligands to target genes. Nat. Methods *17*, 159–162. https://doi.org/10.1038/s41592-019-0667-5.
93. van der Walt, S., Schönberger, J.L., Nunez-Iglesias, J., Boulogne, F., Warner, J.D., Yager, N., Gouillart, E., Yu, T., and scikit-image, c. (2014). scikit-image: image processing in Python. PeerJ *2*, e453. https://doi.org/10.7717/peerj.453.
94. Durinck, S., Spellman, P.T., Birney, E., and Huber, W. (2009). Mapping identifiers for the integration of genomic datasets with the R/Bioconductor package biomaRt. Nat. Protoc. *4*, 1184–1191. https://doi.org/10.1038/nprot.2009.97.
95. Hafemeister, C., and Satija, R. (2019). Normalization and variance stabilization of single-cell RNA-seq data using regularized negative binomial regression. Genome Biol. *20*, 296. https://doi.org/10.1186/s13059-019-1874-1.
96. Stuart, T., Butler, A., Hoffman, P., Hafemeister, C., Papalexi, E., Mauck, W.M., Hao, Y., Stoeckius, M., Smibert, P., and Satija, R. (2019). Comprehensive Integration of Single-Cell Data. Cell *177*, 1888–1902.e21. https://doi.org/10.1016/j.cell.2019.05.031.
97. Benjamini, Y., and Hochberg, Y. (1995). Controlling the False Discovery Rate - a Practical and Powerful Approach to Multiple Testing. J. Roy. Stat. Soc. B *57*, 289–300. https://doi.org/10.1111/j.2517-6161.1995.tb02031.x.
98. Soneson, C., Love, M.I., and Robinson, M.D. (2016). Differential analyses for RNA-seq: transcript-level estimates improve gene-level inferences. F1000Res. *4*, 1521. https://doi.org/10.12688/f1000research.7563.2.
99. Gu, Z., Eils, R., and Schlesner, M. (2016). Complex heatmaps reveal patterns and correlations in multidimensional genomic data. Bioinformatics *32*, 2847–2849. https://doi.org/10.1093/bioinformatics/btw313.
100. Ginestet, C. (2011). ggplot2: Elegant Graphics for Data Analysis. J. Roy. Stat. Soc. *174*, 245–246. https://doi.org/10.1111/j.1467-985X.2010.00676_9.x.
101. Subramanian, A., Tamayo, P., Mootha, V.K., Mukherjee, S., Ebert, B.L., Gillette, M.A., Paulovich, A., Pomeroy, S.L., Golub, T.R., Lander, E.S., and Mesirov, J.P. (2005). Gene set enrichment analysis: a knowledge-based approach for interpreting genome-wide expression profiles. Proc. Natl. Acad. Sci. USA *102*, 15545–15550. https://doi.org/10.1073/pnas.0506580102.
102. Jumper, J., Evans, R., Pritzel, A., Green, T., Figurnov, M., Ronneberger, O., Tunyasuvunakool, K., Bates, R., Žídek, A., Potapenko, A., et al. (2021). Highly accurate protein structure prediction with AlphaFold. Nature *596*, 583–589. https://doi.org/10.1038/s41586-021-03819-2.
103. Varadi, M., Anyango, S., Deshpande, M., Nair, S., Natassia, C., Yordanova, G., Yuan, D., Stroe, O., Wood, G., Laydon, A., et al. (2022). AlphaFold Protein Structure Database: massively expanding the structural coverage of protein-sequence space with high-accuracy models. Nucleic Acids Res. *50*, D439–D444. https://doi.org/10.1093/nar/gkab1061.
104. Castro-Mondragon, J.A., Riudavets-Puig, R., Rauluseviciute, I., Berhanu Lemma, R., Turchi, L., Blanc-Mathieu, R., Lucas, J., Boddie, P., Khan, A., Manosalva Pérez, N., et al. (2022). JASPAR 2022: the 9th release of the open-access database of transcription factor binding profiles. Nucleic Acids Res. *50*, D165–D173. https://doi.org/10.1093/nar/gkab1113.
105. Tirosh, I., Izar, B., Prakadan, S.M., Wadsworth, M.H., 2nd, Treacy, D., Trombetta, J.J., Rotem, A., Rodman, C., Lian, C., Murphy, G., et al. (2016). Dissecting the multicellular ecosystem of metastatic melanoma by single-cell RNA-seq. Science *352*, 189–196. https://doi.org/10.1126/science.aad0501.

STAR★METHODS

KEY RESOURCES TABLE

REAGENT or RESOURCE	SOURCE	IDENTIFIER
Antibodies		
Rabbit monoclonal anti-E-cadherin (clone 24E10)	Cell Signaling Technology	Cat#3195; RRID: AB_2291471
Mouse monoclonal anti-CD138 (SDC1) (clone 44F9)	Miltenyi Biotec	Cat#130-119-928; RRID: AB_2751926
Mouse monoclonal anti-H2A.X (phospho S139) (clone 3F2)	Abcam	Cat#ab22551; RRID: AB_447150
Mouse monoclonal anti-YAP (clone 63.7)	Santa Cruz Biotechnology	Cat#sc-101199; RRID: AB_1131430
Rabbit monoclonal anti-GATA3 (clone D13C9)	Cell Signaling Technology	Cat#5852; RRID: AB_10835690
Rabbit polyclonal anti-hCG beta	Dako	Cat#IR508
Mouse monoclonal anti-hCG beta (clone 5H4-E2)	Abcam	Cat#ab9582; RRID: AB_296507
Mouse monoclonal anti-HLA-G PE-conjugate (clone MEM-G/9)	Abcam	Cat#ab24384; RRID: AB_448029
Rabbit monoclonal anti-Cytokeratin 7 (KRT7) (clone SP52)	Abcam	Cat#ab119697; RRID: AB_10898698
Rabbit monoclonal anti-CD31 (PECAM1) (clone EP3095)	Abcam	Cat#ab134168; RRID: AB_2890012
Rabbit polyclonal anti-cleaved caspase-3 (Asp175)	Cell Signaling Technology	Cat#9661; RRID: AB_2341188
Rabbit monoclonal anti-ITGA2 (clone EPR17338)	Abcam	Cat#ab181548; RRID: AB_2847852
Rabbit monoclonal anti-CREB (phospho S133) (clone E113)	Abcam	Cat#ab32096; RRID: AB_731734
Rabbit monoclonal anti-FOXA2 (clone EPR4466)	Abcam	Cat#ab108422; RRID: AB_11157157
Rabbit polyclonal anti-VEGF Receptor 3 (FLT4)	Abcam	Cat#ab27278; RRID: AB_470949
Rabbit polyclonal anti-RAC1	Abcam	Cat#ab97732; RRID: AB_10679979
Rat monoclonal anti-ITGA6 (CD49f) PE-conjugate (clone GoH3)	BioLegend	Cat#313612; RRID: AB_893373
Goat anti-Rabbit IgG (H + L), F(ab’)2 Fragment Alexa Fluor 488 Conjugate	Cell Signaling Technology	Cat#4412; RRID: AB_1904025
Goat anti-Rabbit IgG (H + L), F(ab’)2 Fragment Alexa Fluor 555 Conjugate	Cell Signaling Technology	Cat#4413; RRID: AB_10694110
Goat anti-Rabbit IgG (H + L), F(ab’)2 Fragment Alexa Fluor 647 Conjugate	Cell Signaling Technology	Cat#4414; RRID: AB_10693544
Goat anti-Mouse IgG (H + L), F(ab’)2 Fragment Alexa Fluor 488 Conjugate	Cell Signaling Technology	Cat#4408; RRID: AB_10694704
Goat anti-Mouse IgG (H + L), F(ab’)2 Fragment Alexa Fluor 555 Conjugate	Cell Signaling Technology	Cat#4409; RRID: AB_1904022
Goat anti-Mouse IgG (H + L), F(ab’)2 Fragment Alexa Fluor 647 Conjugate	Cell Signaling Technology	Cat#4410; RRID: AB_1904023
Biological samples		
Human endometrium and decidua (6–9 weeks of gestation)	Kyono ART Clinic Sendai and Sendai ART Clinic	N/A

(*Continued on next page*)

Continued

REAGENT or RESOURCE	SOURCE	IDENTIFIER
Chemicals, peptides, and recombinant proteins		
DMEM/F12	FUJIFILM Wako	Cat#048-29785
KnockOut Serum Replacement (KSR)	Thermo Fisher Scientific	Cat#10828028
penicillin-streptomycin	Thermo Fisher Scientific	Cat#15140-122
BSA	FUJIFILM Wako	Cat#017-22231
ITS-X	FUJIFILM Wako	Cat#094-06761
L-ascorbic acid	FUJIFILM Wako	Cat#013-12061
EGF	FUJIFILM Wako	Cat#054-09523
BMP4	R&D Systems	Cat#314-BP
CHIR99021	FUJIFILM Wako	Cat#034-23103
A83-01	FUJIFILM Wako	Cat#035-24113
Valproic acid (VPA)	FUJIFILM Wako	Cat#227-01071
Y-27632	FUJIFILM Wako	Cat#036-24023
iMatrix-511	FUJIFILM Wako	Cat#385-07361
SB202190	FUJIFILM Wako	Cat#193-13531
FGF2 (Heat Stable)	Thermo Fisher Scientific	Cat#PHG0369
TrypLE Express	Thermo Fisher Scientific	Cat#12604-021
Accutase	Innovative Cell Technologies	Cat#AT104
Matrigel	Corning	Cat#354234
Novobiocin sodium	Selleck Chemicals	Cat#S2492
Heparin Sodium Salt	Nacalai Tesque Inc.	Cat#17513-41
Phalloidin-iFluor647 conjugate	Abcam	Cat#AB176759
Forskolin	FUJIFILM Wako	Cat#067-02191
Doxycycline hyclate	Sigma-Aldrich	Cat#D9891
Cellmatrix Type I-A	Nitta Gelatin	Cat#631-00651
Concentrated culture solution DF culture solution	Nitta Gelatin	Cat#632-29621
Reconstitution Buffer	Nitta Gelatin	Cat#635-00791
RNase A	QIAGEN	Cat#19101
DQ-Gelatin fluorescein conjugate	Invitrogen	Cat#D12054
FITC-Dextran, 70 kDa	Sigma-Aldrich	Cat#46945
TRITC-Dextran, 4 kDa	Sigma-Aldrich	Cat#T1037
Hoechst 33342	FUJIFILM Wako	Cat#346-07951
Critical commercial assays		
Chromium Single Cell 3′ Reagent Kits v3.1	10× Genomics	Cat#PN-1000268
Chromium Nuclei Isolation Kit	10× Genomics	Cat#PN-1000493
Chromium Next GEM Single Cell Multiome ATAC + Gene Expression kit	10× Genomics	Cat#PN-1000285
EasySep Human PE Positive Selection Kit II	STEMCELL Technologies	Cat#17664
RNeasy Mini Kit	QIAGEN	Cat#74104
RNeasy Micro Kit	QIAGEN	Cat#74004
NEBNext UltraII Directional RNA Library Prep Kit	New England Biolabs	Cat#E7760
NEBNext Ultra II DNA Library Prep Kit	New England Biolabs	Cat#E7645
QIAamp DNA Mini Kit	QIAGEN	Cat#51304
Lenti-X Concentrator	TaKaRa Bio	Cat#631231
Lipofectamine LTX	Thermo Fisher Scientific	Cat#15338100
CalFectin	SignaGen	Cat#SL100478

(*Continued on next page*)

Continued

REAGENT or RESOURCE	SOURCE	IDENTIFIER
PrimeScript II cDNA Synthesis Kit	TaKaRa Bio	Cat#6210 A
StepOnePlus Real-Time PCR System	Thermo Fisher Scientific	Cat#4376600
TB Green Premix Ex Taq II (Tli RNaseH Plus)	TaKaRa Bio	Cat#RR820A
HCG ELISA Kit	Abnova	Cat#KA4005
Deposited data		
snRNA-seq data (hTOr)	This paper	GEO: GSE303893
snRNA-seq data (hTOr_YAP5SA)	This paper	GEO: GSE304580
snRNA-seq data (hTOr–endometrial co-culture)	This paper	GEO: GSE324114
snRNA-seq data (EVT-differentiated hTOr)	This paper	GEO: GSE306469
Single-Cell Multiome data (*AAVS1* KO and *GCM1* KO)	This paper	GEO: GSE305070
Bulk RNA-seq data (hTSC spheroids)	This paper	GEO: GSE324315
Low-pass WGS data	This paper	SRA: PRJNA1432413
Proteomics (LC-MS/MS secretome) data	This paper	PRIDE: PXD075393
First-trimester trophoblast reference	Arutyunyan et al.[25]	ArrayExpress: E-MTAB-12421
Extended human embryonic reference atlas	Zhao et al.[24]	Zenodo: https://zenodo.org/records/12189592
Maternal-fetal interface atlas	Vento-Tormo et al.[36]	ArrayExpress: E-MTAB-6701
Human GCM1 structure	AlphaFold Protein Structure DB	AF-Q9NP62-F1-model_v4
Drosophila GCM domain structure	Protein DataBank	PDB: 1ODH
Experimental models: Cell lines		
Human: Lenti-X^{TM} 293 T cell Line	TaKaRa Bio	Cat#632180; RRID: CVCL_4401
Human: TSC line (B31)	Shimizu et al.[43]	N/A
Human: TSC lines (CT27, and CT29)	Okae et al.[12]	CT27: CVCL_A7AZ; CT29: CVCL_A7BA
Human: RFP-HUVEC	Angioproteomie	Cat#cAP-0001RFP
Human: HUVEC	TaKaRa Bio	Cat#D10011
Human: Endometrial organoids (hEMO)	Shibata et al.[21]	N/A
Human: GFP-expressing hEMO	Shibata et al.[21]	N/A
Human: KuO-expressing hTSCs	Hori et al.[18]	N/A
Human: *GCM1* KO/*AAVS1* KO hTSCs	Shimizu et al.[43]	N/A
Human: YAP5SA hTSC line	This paper	N/A
Oligonucleotides		
Primers used in this study, see Table S2	This paper	N/A
sgRNA sequences for GCM1 and AAVS1 targeting	Shimizu et al.[43]	N/A
Recombinant DNA		
pTetOne	TaKaRa Bio	Cat#634301
CS-CA-MCS	H. Miyoshi, RIKEN BRC	Cat#RDB05963
pQCXIH-Myc-YAP-5SA	Zhao et al.[69]; Addgene	Addgene plasmid #33093
pCMV-VSV-G-RSV-Rev	H. Miyoshi, RIKEN BRC	Cat#RDB04393
pCAG-HIV-gp	H. Miyoshi, RIKEN BRC	Cat#RDB04394
pCS-CA-Tet3G	Takahashi et al.[70]	N/A
pCS-3G	Takahashi et al.[70]	N/A
pCS-3G-YAP5SA	This paper	N/A
Software and algorithms		
R (v4.3.0/v4.3.1)	R Core Team	https://www.r-project.org/; RRID: SCR_001905
Seurat (v4.3.0/v4)	Hao et al.[71]	https://satijalab.org/seurat/

(*Continued on next page*)

Continued

REAGENT or RESOURCE	SOURCE	IDENTIFIER
Signac	Stuart et al.[72]	https://stuartlab.org/signac/
Cell Ranger (v8.0.1) and Cell Ranger ARC	10× Genomics	https://support.10xgenomics.com
scVelo (v0.2.5)	Bergen et al.[73]	https://scvelo.readthedocs.io/
velocyto (v0.17.17)	La Manno et al.[74]	http://velocyto.org/
Monocle3 (v1.3.1)	Cao et al.[75]	https://cole-trapnell-lab.github.io/monocle3/
clusterProfiler (v4.8.0)	Yu et al.[76]	Bioconductor
BWA-MEM2 (v2.2.1)	Vasimuddin et al.[77]	https://github.com/bwa-mem2/bwa-mem2
samtools (v1.23)	Li et al.[78]	http://www.htslib.org/
QDNAseq (v1.40.0)	Scheinin et al.[79]	Bioconductor
STAR (v2.7.11 b)	Dobin et al.[80]	https://github.com/alexdobin/STAR
TrimGalore (v0.6.7)	Felix Krueger	https://github.com/FelixKrueger/TrimGalore
RSEM (v1.3.3)	Li and Dewey[81]	https://deweylab.github.io/RSEM/
chromVAR	Schep et al.[82]	Bioconductor
Slingshot	Street et al.[83]	Bioconductor
tricycle	Zheng et al.[84]	Bioconductor
DESeq2	Love et al.[85]	Bioconductor
GraphPad Prism (v10.0.2)	GraphPad Software	https://www.graphpad.com/; RRID: SCR_002798
ImageJ/Fiji	Schneider et al.[86]	https://imagej.net/; RRID: SCR_002285
VIPER	Alvarez et al.[87]	Bioconductor; https://www.bioconductor.org/packages/release/bioc/html/viper.html
DoRothEA	Garcia-Alonso L et al.[88]	Bioconductor; https://saezlab.github.io/dorothea/
PROGENy	Schubert et al.[89]	Bioconductor; https://saezlab.github.io/progeny/
Cellpose	Stringer et al.[90]	https://www.cellpose.org/; RRID: SCR_021553
Imaris software	Bitplane	https://imaris.oxinst.com/; RRID: SCR_007370
BZ-X Analyzer	Keyence	https://www.keyence.com/
PyMOL	Schrödinger, LLC	https://pymol.org/; RRID: SCR_000305
DIA-NN (v1.8.1)	Demichev et al.[91]	https://github.com/vdemichev/DiaNN
NicheNet	Browaeys et al.[92]	https://github.com/saeyslab/nichenetr
scikit-image	van der Walt et al.[93]	https://scikit-image.org/
Other		
AggreWell 400 24-well plates	STEMCELL Technologies	Cat#34411
ClinoStar bioreactor	CelVivo	N/A

EXPERIMENTAL MODEL AND STUDY PARTICIPANT DETAILS

Ethics statement and human tissue-derived organoids

This study used previously established human endometrial organoid (hEMO) cultures, including GFP-expressing hEMO, generated from female donor-derived human endometrial and first-trimester decidual tissues as described previously.[21] Decidual tissue sources were from 6 to 9 weeks of gestation where applicable. No new primary human endometrial or decidual tissue collection was performed solely for the present study. Patient age information for the donor-derived hEMO resource was not available for analysis. Samples were de-identified before use. All donors were recruited at collaborating clinical sites in Japan; donor gender identity, ancestry, race, and ethnicity were not systematically collected. All experimental protocols and procedures were approved by the Ethics Committee of the Tohoku University Graduate School of Medicine (2022-1-704). Sample sizes for individual assays are provided in the corresponding figure legends.

Sex as a biological variable

For hTSC lines, sex refers to the fetal/placental sex of the conceptus or tissue of origin. The hTSC lines used in this study included B31 (46,XX, female; blastocyst-derived[43]), CT27 (46,XX, female; first-trimester cytotrophoblast-derived; CVCL_A7AZ), and CT29 (46,XY, male; first-trimester cytotrophoblast-derived; CVCL_A7BA). Sex annotations for CT27 and CT29 are based on Okae et al.[12] and associated cell-line records; the B31 line was originally described in Shimizu et al.[43] as a blastocyst-derived hTSC line. The hEMO cultures used in this study were derived from female donor reproductive tissues. Although both female- and male-derived hTSC lines were included, this study was not designed or powered to assess sex-associated effects because the number of independent lines per sex was limited and sex was confounded with donor/cell-line identity. Therefore, sex or gender was not included as a variable in the statistical analyses.

Human trophoblast stem cell lines and derived trophoblast organoids

Human trophoblast stem cell (hTSC) lines (species: Homo sapiens) included B31, CT27, CT29, AAVS1 KO hTSCs, and GCM1 KO hTSCs (originally described in Okae et al.12 and Shimizu et al.43). hTSC lines and engineered derivatives were maintained as previously described,[12,43,70] authenticated by expected morphology, trophoblast lineage-marker expression, and genotype- or transgene-specific validation where applicable, and tested negative for mycoplasma contamination by PCR.

Human endometrial organoids

Human endometrial organoids (hEMO), including GFP-expressing hEMO, were previously generated from female donor-derived human endometrial and first-trimester decidual tissues as described above and in Shibata et al.[21] These primary human epithelial organoid cultures were used for hTOr–hEMO co-culture and hTOr-conditioned-medium experiments. hEMO cultures were maintained and experimentally allocated as described in Method Details.

HUVECs and 293 T cells

RFP-HUVECs were purchased from Angioproteomie (Boston, MA), and HUVECs were obtained from TaKaRa Bio. HUVECs are derived from neonatal umbilical vein tissue; donor sex was lot-specific and not disclosed by the suppliers. HUVECs were used for trophoblast-endothelial co-culture assays. Human 293 T cells were obtained from TaKaRa Bio (Kyoto, Japan) and used for lentiviral vector production; the parental HEK293 line was derived from a female embryonic kidney. Cell lines were maintained according to supplier recommendations, authenticated by supplier documentation and expected morphology, and tested negative for mycoplasma contamination by PCR.

METHOD DETAILS

hTSC culture

hTSCs were maintained as previously described[12,43,70] in DMEM/F12 supplemented with 1% KnockOut Serum Replacement (KSR), 0.5% penicillin-streptomycin, 0.15% BSA, 1% ITS-X, 200 μM L-ascorbic acid, 25 ng/mL EGF, 10 ng/mL BMP4, 2 μM CHIR99021, 5 μM A83-01, 0.8 mM valproic acid, and 2.5 μM Y27632. Cells were cultured on iMatrix-511–coated plates (0.5 μg/mL, Nippi) at 37°C, 5% CO_2. Medium was replaced every 2 days. *AAVS1* KO and *GCM1* KO hTSCs were established as described previously and maintained similarly.[43,70]

Spheroid formation assay (factor drop-out)

To optimize culture medium, hTSCs were seeded into low-attachment 96-well U-bottom plates (100 cells/well) in either full ECSY medium or medium lacking individual components (-E, -C, -S, -Y). After 24 h, spheroid morphology was assessed by phase-contrast microscopy and categorized as Good (compact, spherical), Moderate (irregular aggregates), or Bad (dispersed cells).

Generation of hTSC spheroids and rotation-cultured human trophoblast organoids (hTOr)

hTSCs were dissociated and seeded onto AggreWell 400 24-well plates (Stem Cell Technologies) at 6×10^5 cells/well in ECSY medium (DMEM/F-12, 1% ITS-X, 0.15% BSA, 1% KSR, 200 μM L-ascorbic acid, 50 ng/mL EGF, 2 μM CHIR99021, 2 μM SB202190, and 10 μM Y27632). After 24 h, spheroids were collected, filtered through a 200 μm cell strainer to eliminate aggregates, and transferred to different 3D culture conditions for comparative studies. Rotational culture was performed using a ClinoStar bioreactor (CelVivo) at 37°C with 5% CO_2. Organoids were maintained under continuous rotation with speed adjusted to organoid size (9–11 rpm for days 1–3, 10–13 rpm for days 3–7, and 13–20 rpm for days 7–15) to maintain central suspension. The culture medium was ECSY supplemented with 50 ng/mL FGF2 (Heat Stable, Thermo Fisher Scientific), 1 μg/mL heparin, and 20 ng/mL BMP4, with Y27632 concentration reduced to 2.5 μM (from the original 10 μM in ECSY medium). Additional culture conditions included floating culture in non-treated 100 mm dishes without agitation, shaking culture in non-treated 100 mm dishes with horizontal agitation using a MINI SHAKER MS-LR (AS ONE, Tokyo, Japan) at maximum speed, and Matrigel-embedded culture using Matrigel (Corning). Organoid growth was monitored daily by phase-contrast and bright-field microscopy, with organoid diameter and lumen area measured using BZ-X Analyzer (Keyence).

Immunofluorescence staining and imaging

Samples were fixed in 4% paraformaldehyde for 30 min at room temperature and washed three times with PBS. For cryosectioning, samples were incubated overnight at 4°C in 30% sucrose in PBS, embedded in Tissue-Tek O.C.T. compound (Sakura Finetek, Tokyo, Japan), snap-frozen in liquid nitrogen, and sectioned at 10 μm thickness using a cryostat. Cells, intact organoids, or frozen sections were permeabilized and blocked in 5% normal goat serum and 0.3% Triton X-100 in PBS for 1 h at room temperature. Samples were then incubated with primary antibodies (see Key Resources Table) overnight at 4°C, followed by Alexa Fluor–conjugated secondary antibodies for 1 h at room temperature. Nuclei were counterstained with Hoechst 33342, and F-actin was visualized using a Phalloidin-iFluor 647 Reagent (Abcam). Images were acquired using a BZ-X810 fluorescence microscope (Keyence) or an LSM780 confocal microscope (Zeiss).

Quantification of syncytiotrophoblast surface coverage

To quantify the surface coverage of the outer syncytiotrophoblast layer, 3D surface rendering of whole-mount immunofluorescence images was performed using Imaris software (Bitplane). Surfaces were created for SDC1 (syncytiotrophoblast) and E-cadherin (cytotrophoblast) channels based on fluorescence intensity thresholds. The STB Coverage (%) was calculated as the ratio of the SDC1-positive surface area to the total surface area (defined as the sum of SDC1-positive and E-cadherin-positive areas).

Permeability barrier assay

Barrier function was assessed by measuring the exclusion of fluorescent dextrans. Day-11 hTOr and control hTOm (Matrigel-cultured) were transferred to 8-well chamber slides and incubated with a mixture of FITC-dextran (70 kDa, 1 mg/mL; Sigma-Aldrich) and TRITC-dextran (4 kDa, 0.5 mg/mL; Sigma-Aldrich) in culture medium for 1 h at 37°C. After incubation, organoids were imaged immediately without washing using a Zeiss LSM780 confocal microscope. Image analysis was performed using ImageJ (Fiji).[86] The infiltration rate was calculated as the ratio of the fluorescence-positive area to the total organoid cross-sectional area. Maximum and mean infiltration depths were measured from the organoid surface toward the center.

Quantification of apoptosis

Apoptosis within trophoblast organoids was quantified using immunofluorescence images of frozen sections stained for cleaved caspase-3. Images were processed and analyzed using the BZ-X Analyzer software (Keyence). The total number of nuclei (Hoechst-positive) and apoptotic cells (cleaved caspase-3-positive) were automatically counted using the cell counting function after applying uniform fluorescence intensity thresholds. The apoptosis rate was calculated as the percentage of cleaved caspase-3-positive cells relative to the total number of nuclei per organoid section.

Transmission electron microscopy (TEM)

Transmission electron microscopy was performed to analyze organoid ultrastructure. Organoids were pre-fixed at room temperature, sectioned, and washed with 0.1 M cacodylate buffer containing 8% sucrose on ice. Post-fixation was performed with 1% osmium tetroxide on ice for 90 min, followed by buffer washes. Samples were dehydrated through a graded ethanol series (50–100%) and treated with propylene oxide before sequential infiltration with Epon resin using stepwise propylene oxide/resin ratios. The resin mixture contained MNA, DDSA, Epon 812, and DMP-30 in standard proportions. Embedding was completed overnight at 30°C, followed by polymerization at 60°C for 2–3 days. Semi-thin sections (200–300 nm) were cut using a Leica EM UC7 ultramicrotome, mounted, and stained with toluidine blue for light microscopic evaluation and region selection. Ultrathin sections (80 nm) were cut, mounted on grids, and stained sequentially with 2% uranyl acetate and lead citrate mixture. Sections were examined using a JEOL JEM-1400 transmission electron microscope.

Organoid passaging

To passage hTOr, day 11 organoids were dissociated into single cells using TrypLE Express (Thermo Fisher Scientific) for up to 15 min at 37°C. The reaction was stopped with PBS containing 2% FBS, followed by centrifugation. For progenitor enrichment, ITGA6$^+$ cells were isolated using the EasySep Human PE Positive Selection Kit II (STEMCELL Technologies). Briefly, dissociated cells were resuspended in PBS/2% FBS, filtered through a 40-μm strainer, and blocked with FcR blocker. Cells were then stained with PE-conjugated anti-ITGA6 antibody for 15 min at room temperature. After washing, cells were incubated with the Selection Cocktail (15 min) and RapidSphere magnetic beads (10 min). The suspension was placed in an EasySep Magnet for 5 min, and the supernatant containing non-labeled cells was discarded. This magnetic separation step was repeated once to maximize purity. The retained ITGA6$^+$ cells were resuspended in ECSY medium, counted, and re-seeded into AggreWell 400 plates at a density of 6×10^5 cells/well. Plates were centrifuged at 100 × g for 3 min to aggregate cells. After 24 h, reformed spheroids were transferred to rotational culture.

snRNA-seq and analysis

Single nuclei were isolated using the Chromium Nuclei Isolation Kit (10× Genomics), and approximately 10,000 nuclei per sample were used to generate dual-indexed libraries with Chromium Single Cell 3′ Reagent Kits v3.1. Libraries were sequenced on an Illumina NovaSeq X Plus (150 bp paired-end reads) and aligned using Cell Ranger v8.0.1 with the GRCh38-2020-A-2.0.0 reference genome. Raw UMI matrices were analyzed in R v4.3.0 using Seurat v4.3.0. Quality control parameters were optimized based on sample characteristics and analytical objectives. For high-resolution profiling (e.g., organoid characterization), cells with 800–10,000 detected genes, <60,000 UMIs, <7.5% mitochondrial, and <3% ribosomal RNA were retained. For comparative or perturbation studies, relaxed thresholds (200–6,000 genes, <10% mitochondrial/ribosomal RNA) were applied. For cross-platform validation analyses, technology-specific criteria were employed: >500 genes for 10× and >1,000 genes for Smart-seq2, both with <20% mitochondrial content. Ribosomal genes were excluded using the pattern ' ˆRP[SL][[:digit:]]| ˆRPLP[[:digit:]]| ˆRPSA'.

Cell cycle analysis

Cell cycle phase assignment was performed using Seurat's CellCycleScoring() with canonical gene sets (cc.genes.updated.2019) converted to Ensembl IDs via biomaRt[94] to ensure platform compatibility. Assignment was conducted prior to normalization and integration to support downstream interpretation of proliferative states.

Normalization and integration

Normalization was performed using SCTransform,[95] with regression of technical covariates (nFeature_RNA, nCount_RNA, percent.mt, percent.rb) for developmental profiling, or minimal regression (percent.mt only) in perturbation settings. Integration followed Seurat's anchor-based SCTransform pipeline[96] for direct dataset comparisons. Variable features (3,000–3,500) were selected via SelectIntegrationFeatures().

Dimensionality reduction and clustering

Dimensionality reduction used RunPCA() (20–30 PCs), with elbow plots guiding selection. UMAP embeddings were computed from the top 12 PCs (n.neighbors = 30, min.dist = 0.3–0.5), and graph-based clustering was performed (FindNeighbors(), FindClusters() at resolution 0.3–0.5). Cell identities were annotated via canonical markers and validated against published atlases. Cluster-specific markers were identified using FindAllMarkers() (only.pos = TRUE, min.pct = 0.25, logfc.threshold = 0.25, adjusted $p < 0.05$). Differential expression used FindMarkers() with thresholds adjusted $p < 0.05$ and $|\log_2 FC| > 0.5$.

Label transfer and cell type prediction

To systematically annotate hTOr cell types, we utilized the first-trimester trophoblast single-nucleus RNA-seq dataset from Arutyunyan et al. (2023)[25] as a reference. Both datasets were normalized using SCTransform. Integration anchors were identified using FindTransferAnchors (normalization.method = "SCT", dims = 1:30). Cell type labels ("final_annot_all_troph_corrected") were projected onto the hTOr dataset using TransferData. Prediction scores were calculated to assess confidence.

RNA velocity and pseudotime analysis

RNA velocity was inferred using scVelo[73] (v0.2.5). Spliced/unspliced matrices were generated via velocyto[74] (v0.17.17) from Cell Ranger BAMs. Preprocessing included filtering, normalization, and PCA-based neighbor graph construction (30 PCs, 30 neighbors). Velocities were computed using the dynamical model and projected onto Seurat-derived UMAP coordinates. Latent time ordering was used to visualize progression across differentiation trajectories. Pseudotime analysis was performed using Monocle3[75] (v1.3.1) on converted Seurat objects. Graph-based trajectory inference (learn_graph) and cell ordering (order_cells) defined developmental hierarchies. RNA velocity trajectories were overlaid to validate directionality.

Projection onto the extended human embryonic reference

To determine developmental stage, hTOr snRNA-seq data were projected onto an extended human embryonic reference atlas (Zhao et al.,[24]). Briefly, hTOr count matrices were aggregated with miloR to enhance sparsity, cosine-normalized, and projected into the reference batch-corrected PCA space using lineage-specific mutual nearest neighbor (MNN) vectors (batchelor). Developmental affinity was quantified by identifying MNNs between query and reference cells, classifying each hTOr cell as either "Embryonic" (E5–E14) or "First Trimester" based on its nearest neighbor in the reference manifold.

Maturation score and gene correlation

A maturation score was calculated for each hTOr cell as the mean developmental stage of its mutual nearest neighbors in the reference atlas. Spearman correlation analysis was performed between gene expression and maturation scores to identify lineage-specific maturation markers. For visualization, expression values were smoothed using a moving average filter and Z score normalized.

Inference of transcription factor and pathway activities

Transcription factor (TF) activities were inferred from gene expression data using the DoRothEA regulon database and VIPER algorithm (dorothea R package).[87,88] Signaling pathway activities were estimated using PROGENy,[89] which computes pathway scores based on the expression of downstream responsive genes. Spearman correlation coefficients were calculated between these activity scores and maturation scores to identify stage-specific regulators.

Force-directed network topology analysis

To visualize GRN restructuring by YAP5SA, we constructed a physics-based interaction network. Top 10 activated and suppressed TFs were identified using VIPER, and their differentially expressed target genes were mapped. The network layout was computed using the Fruchterman-Reingold force-directed algorithm (ggraph), where node proximity reflects connectivity. Convex hulls were used to demarcate functionally distinct regulatory domains.

Target prioritization and waterfall visualization

To dissect the underlying regulatory mechanism, we constructed a focused regulatory network. We filtered for target genes that were (1) upregulated in YAP5SA ($\text{Log}_2\text{FC} > 0.25$), (2) activated by YAP-associated TFs (top 10 active), and (3) repressed by Control-associated TFs (top 10 suppressed). The network was visualized using a sorted waterfall layout (ggraph) to illustrate the hierarchy of regulation.

Functional enrichment and semantic clustering

GO enrichment analysis (Biological Process) was performed on YAP-driven targets using clusterProfiler (p-adjust <0.05). To resolve term redundancy, semantic similarity analysis was conducted using enrichplot. Pairwise similarity matrices were computed (Resnik method) and hierarchically clustered (Ward's method) to generate a "Functional Tree," visualizing dominant biological programs.

Phase-space trajectory analysis

Continuous cell cycle position (θ) was estimated using the tricycle R package.[84] Differentiation pseudotime was inferred using Slingshot.[83] Single cells were plotted in a 2D phase-space defined by pseudotime and cell cycle phase to visualize the coupling between differentiation and proliferation.

Functional module scoring and trajectory analysis

To evaluate metabolic reprogramming in the endometrial organoid (hEMO) co-culture model, metabolic pathway activity was quantified at the single-cell level using the AddModuleScore function in Seurat. Specifically, gene sets for Oxidative Phosphorylation (OXPHOS) and Glycolysis were derived from the MSigDB Hallmark collection (Table S1).

Statistical analysis and enrichment

Gene Ontology enrichment was performed using clusterProfiler[76] v4.8.0 and org.Hs.e.g.,.db. Gene symbols were converted to Entrez IDs using bitr() and enrichGO() was run for Biological Process terms with Benjamini-Hochberg correction[97] ($p < 0.05$, FDR $q < 0.2$). Statistical comparisons used one-way ANOVA with Tukey's HSD or non-parametric alternatives when assumptions were violated. Correlation coefficients were computed with Spearman's rank test ($p < 0.05$).

In situ gelatinase activity assay

To visualize proteolytic activity, hTOr at day 11 were incubated with DQ-Gelatin fluorescein conjugate (Invitrogen, D12054). Organoids were transferred to non-treated 4-well plates containing 100 µg/mL DQ-Gelatin in ECSY + BF medium. After 24 h of incubation at 37°C, organoids were washed twice with PBS to remove background fluorescence and imaged using a BZ-X810 (Keyence). Fluorescein signal generated by gelatin cleavage was captured to assess the spatial localization of gelatinase activity.

γH2AX-focus formation and nuclear morphology assay

POLQ inhibition assays were performed using novobiocin sodium (Selleck, #S2492) at 50 and 100 µM with DMSO vehicle control. hTSCs were seeded in iMatrix-511–coated 24-well plates at different densities: 3.9×10^4 cells/well for γH2AX analysis (treated after 48 h culture) or 9.8×10^3 cells/well for nuclear morphology analysis (treated immediately upon seeding). Cells were fixed with 4% paraformaldehyde for 30 min at 6 and 24 h (γH2AX assay) or 72 h (nuclear morphology assay) post-treatment. For both assays, quantitative analysis was performed using an image cytometer (BZ-H4XI). For γH2AX analysis, immunofluorescence-stained cells were evaluated with results expressed as γH2AX foci per Hoechst-stained nucleus. For nuclear morphology analysis, nuclear area and perimeter measurements were obtained from Hoechst-stained cells, and circularity was calculated as $(4\pi \times \text{Area})/(\text{Perimeter}^2)$ with nuclei categorized as normal (≥ 0.8) or abnormal (< 0.8). Outliers were removed using the 1.5×IQR method. Statistical comparisons used Kruskal-Wallis test with Dunn's post-hoc correction, conducted in R.

Low-pass whole genome sequencing (WGS) and CNA analysis

Genomic DNA was extracted from hTOr using the QIAamp DNA Mini Kit (QIAGEN), following the manufacturer's protocol with minor modifications. Briefly, organoids were homogenized in Buffer ATL and digested with Proteinase K at 56°C until complete lysis. To remove RNA contamination, lysates were treated with RNase A (100 mg/mL, QIAGEN) for 2 min at room temperature. DNA was purified using QIAamp Mini Spin Columns, washed with Buffer AW1 and AW2, and eluted in nuclease-free water. DNA concentration and purity were determined using a NanoDrop spectrophotometer (Thermo Fisher Scientific). Library preparation and whole genome sequencing were performed on an Illumina NovaSeq X Plus platform (150-bp paired-end reads) targeting 1–3 Gb per sample (approximately 1× coverage). Sequencing libraries were prepared using the NEBNext Ultra II DNA Library Prep Kit (New England Biolabs).

For Copy Number Alteration (CNA) analysis, raw reads were aligned to the human reference genome (GRCh38/hg38) using BWA-MEM2 (v2.2.1)[77] and sorted with samtools (v1.23).[78] Copy number analysis was performed using the QDNAseq R package (v1.40.0)[79] with a bin size of 100 kb. GC content correction was omitted to preserve biological signals inherent to low-coverage data. CNA segments were defined by merging consecutive bins that exhibited a $\log_2$ ratio difference of less than 0.1. Genomic instability was quantified by calculating the Median Absolute Deviation (MAD) score (defined as the median absolute deviation of $\log_2$ ratios) and the Fraction of Genome Altered (FGA) (defined as the proportion of bins with an absolute $\log_2$ ratio >0.2). Segment length distributions between groups were statistically compared using the Kolmogorov-Smirnov test.

Bulk RNA-seq and analysis

Total RNA was extracted using the RNeasy Micro Kit (QIAGEN) with genomic DNA removal by ribonuclease-free deoxyribonuclease I. Libraries were prepared using the NEBNext UltraII Directional RNA Library Prep Kit (New England Biolabs) and sequenced on Illumina NovaSeq X Plus (150-bp paired-end reads). Raw reads were quality-trimmed using TrimGalore (v0.6.7) with 10-bp 5′ clipping and adapter removal, then aligned to GRCh38/hg38 using STAR[80] (v2.7.11 b) with RefSeq annotation and transcript quantification mode. Transcript abundance was quantified using RSEM[81] (v1.3.3) with strand-specific parameters, generating TPM and raw read counts. Gene symbols were mapped from Ensembl IDs using org.Hs.e.g.,.db. Count matrices were imported via tximport[98] and analyzed with DESeq2.[85] Samples were grouped by culture condition (rotation, Matrigel, floating, shaking) with biological replicates from two hTSC lines (B31, CT27). Variance-stabilizing transformation was applied for downstream analyses. Genes with adjusted $p < 0.05$ (Benjamini-Hochberg correction) and $|\log_2 FC| > 1.0$ were considered significantly differentially expressed. Principal component analysis and sample correlation analysis were performed on variance-stabilized data using the top 500 most variable genes. Visualizations included hierarchical clustering heatmaps (pheatmap), correlation matrices (ComplexHeatmap[99]), volcano plots (ggplot2[100]), and expression profiles with averaged TPM values. Gene Ontology enrichment analysis was performed using clusterProfiler (v4.8.0)[76] for Biological Process terms with Benjamini-Hochberg correction (adjusted $p < 0.05$, FDR $q < 0.05$).

Gene set enrichment analysis (GSEA)

To assess YAP/TEAD transcriptional activity, genes were ranked by the $\log_2$ fold change in expression between Matrigel-embedded cultures ($n = 2$) and all other conditions (Rotation, Floating, Shaking; $n = 6$). The ranking metric was defined as $\log_2(\text{Mean TPM\_Matrigel} + 1) - \log_2(\text{Mean TPM\_Others} + 1)$. GSEA was performed using R (10,000 permutations) based on the original GSEA method,[101] against the "Conserved YAP/TAZ signature" gene set defined by Zanconato et al.[39]

Inference of transcription factor activity and GRN construction

TF activities were inferred from variance-stabilized RNA-seq counts using VIPER with high-confidence DoRothEA regulons (levels A–C). To identify "Hub TFs," we selected TFs that satisfied two criteria: (1) regulation of STB functional genes (hormones, fusogens, transporters) in DoRothEA, and (2) significantly higher activity in rotational culture ("Rotation Dominance," FDR <0.25). The Gene Regulatory Network (GRN) was constructed by integrating transcriptional interactions (DoRothEA) with protein-protein interactions (STRINGdb, score >700). Network visualization was performed using ggraph, with node size scaled to significance ($-\log_{10}$ FDR) and color indicating rotation dominance.

Quantification of spatial fluorescence distribution

To quantify the spatial distribution of pCREB, fluorescence intensity profiles were measured across the diameter of equatorial optical sections using ImageJ (Fiji). Profile lengths were spatially normalized to a standard scale (0–100%) by linear interpolation. Fluorescence intensities were aggregated from $n = 10$ organoids to calculate the mean spatial distribution and standard deviation using R.

Generation of doxycycline-inducible YAP5SA hTSC line

A doxycycline-inducible YAP5SA expression system was established using dual lentiviral vectors. The Tet-On 3G transactivator from pTetOne (Takara) was amplified and inserted into CS-CA-MCS (H. Miyoshi, RIKEN BioResource Center), yielding pCS-CA-Tet3G. The CAG promoter in CS-CA-MCS was subsequently replaced with the TRE3Gs promoter from pTetOne to generate pCS-3G.[70] Myc-tagged YAP5SA, amplified from pQCXIH-Myc-YAP-5SA (Addgene #33093),[69] was integrated into pCS-3G, producing pCS-3G-YAP5SA. Lentiviral particles were generated by co-transfecting 293 T cells (Takara Bio) with pCS-CA-Tet3G and pCS-3G-YAP5SA alongside packaging vectors pCMV-VSV-G-RSV-Rev and pCAG-HIV-gp (H. Miyoshi) using Lipofectamine LTX (Thermo Fisher Scientific) or CalFectin (Signagen). Forskolin (10 μM) was supplemented 24 h post-transfection, and viral supernatants were harvested at 72 h and concentrated using Lenti-X Concentrator (Takara Bio).

For gain-of-function studies, hTSCs were sequentially transduced with Tet-On 3G and YAP5SA lentiviruses. YAP5SA expression was induced by adding 100 ng/mL doxycycline (Sigma-Aldrich) during rotation culture, while control conditions excluded doxycycline treatment. Primer sequences are provided in Table S2.

2D monolayer culture and serial passaging analysis

To assess YAP5SA effects under standard adherent culture conditions, CT27_YAP5SA cells were maintained in 2D monolayer culture on tissue culture-treated polystyrene surfaces. Two independent serial passaging experiments were conducted over 23–24 cumulative culture days. Cells were initially seeded at 50,000–100,000 cells per well and passaged every 3–4 days upon reaching approximately 80% confluence. At each passage, cells were dissociated using TrypLE Express (Gibco), and viable cell numbers were determined using an automated cell counter (Cell Counter model R1, Olympus). Population doubling levels (PDL) were calculated as the base 2 logarithm of the ratio of total cumulative cell yield to initial cell number, accounting for all previous passage dilutions. Serial dilution ratios ranged from 1:10 to 1:32 depending on cell density. Growth kinetics were assessed by plotting cumulative PDL against culture days.

Structural modeling and visualization

The human GCM1-DNA complex model was constructed using homology modeling based on the experimental crystal structure of the Drosophila melanogaster GCM domain bound to DNA (PDB: 1ODH; 1.95 Å resolution).[45] The human GCM1 structure was obtained from the AlphaFold Protein Structure Database[102,103] (AF-Q9NP62-F1-model_v4). Structural alignment was performed using PyMOL (Schrödinger, LLC), aligning the DNA-binding domain region (residues 14–169) of human GCM1 with the corresponding region of the Drosophila GCM structure. The alignment yielded an RMSD of 0.463 Å, indicating exceptionally high structural conservation between species. The theoretical DNA-protein complex was generated by superimposing the human GCM1 AlphaFold model onto the Drosophila GCM-DNA crystal structure, with DNA coordinates (chains C and D) retained from the template structure. For visualization, Exon 3 (residues 19–102) was highlighted in green, other protein regions in black, and DNA in red using cartoon representation. All molecular graphics were rendered using PyMOL.

Single-cell multiome analysis

Single nuclei were isolated from organoids as described in the snRNA-seq section. Approximately 10,000 nuclei were loaded onto a 10× Genomics Chromium Controller, and single-cell libraries were prepared using the Chromium Next GEM Single Cell Multiome ATAC + Gene Expression kit according to manufacturer specifications, enabling simultaneous profiling of chromatin accessibility and gene expression from individual nuclei. Raw sequencing data were processed using Cell Ranger ARC (10× Genomics) to generate filtered feature-barcode matrices. Data analysis was performed in R (v4.3+) using Seurat (v4)[96] and Signac[72] packages. For RNA data, cells were filtered to retain nuclei with 200-6,000 detected genes, <10% mitochondrial gene expression (ˆMT-), and <10% ribosomal protein gene expression (RP[SL]|RPLP|ˆRPSA). For ATAC data, peaks were restricted to canonical chromosomes (chr1-22, X, Y), and cells with TSS enrichment scores <2 were excluded. Only cells passing quality control in both modalities were retained for downstream analysis.

Normalization and multimodal integration

RNA data were normalized using SCTransform,[95] followed by principal component analysis (PCA). ATAC data were normalized using term frequency-inverse document frequency (TF-IDF) transformation and subjected to singular value decomposition (SVD) for latent semantic indexing (LSI). Weighted nearest neighbor (WNN) integration was performed using FindMultiModalNeighbors,[71] incorporating PCA dimensions 1–30 from RNA and LSI components 2–30 from ATAC data. Unified UMAP embedding was generated from the WNN graph, and clusters were identified by graph-based clustering at resolution 0.4.

Pseudotime trajectory analysis

To reconstruct the developmental trajectory of trophoblast differentiation, we performed pseudotime analysis based on the global transcriptomic and chromatin-accessibility profiles. A shared trajectory axis was defined using the first principal component (PC1) of the integrated object or inferred using Slingshot, rooted at the *TP63*-high cytotrophoblast (CTB) population. The pseudotime values were normalized to a scale of 0–100, representing the progression from stem-like state to differentiated state (or pathological state in KO). To visualize TF activity dynamics along differentiation, ChromVAR deviation scores for key transcription factors were plotted against pseudotime and smoothed using Local Polynomial Regression Fitting (LOESS) with 95% confidence intervals.

TF target module analysis

To assess whether TF chromatin activity translates into downstream gene expression, we computed target module scores for key transcription factors. TF-target relationships were obtained from the CollecTRI and DoRothEA databases (confidence levels A, B, C). To identify context-relevant functional targets, database-defined targets were intersected with differentially expressed genes between Control and *GCM1* KO organoids: for "lost" TFs (GCM1, CREB1, CEBPB), targets significantly downregulated in KO (adjusted $p < 0.05$, $\log_2 FC < -0.5$) were retained; for "gained" TFs (KLF4, KLF5, MAZ, GATA6), targets significantly upregulated in KO (adjusted $p < 0.05$, $\log_2 FC > 0.5$) were retained. Module scores were calculated as the mean Z-scored expression of filtered target genes per cell.

To examine the relationship between TF chromatin accessibility and target gene expression at single-cell resolution, ChromVAR deviation scores (motif accessibility) were plotted against target module expression scores for each cell. Trends for each genotype were visualized using LOESS regression with 95% confidence intervals.

Differential gene expression analysis

Cluster-specific marker genes were identified using FindAllMarkers on the SCT assay (min.pct = 0.1, logfc.threshold = 0.25). Differential expression between specific clusters was assessed using FindMarkers with Wilcoxon rank-sum test. Gene Ontology enrichment analysis was performed using clusterProfiler[76] with org.Hs.e.g.,.db annotation, applying Benjamini-Hochberg correction[97] (adjusted p-value <0.05).

Chromatin accessibility and motif analysis

Transcription factor motif accessibility was quantified using chromVAR.[82] Position frequency matrices for human transcription factors were obtained from JASPAR2022 database[104] and added to the Seurat object using AddMotifs with BSgenome.Hsapiens.UCSC.hg38 as reference genome. Motif deviation z-scores were calculated using RunChromVAR, quantifying relative accessibility of specific TF binding sites across individual cells. Differential motif accessibility between clusters was assessed using FindMarkers on the chromvar assay, and top motifs were visualized using DotPlot and heatmaps (pheatmap, viridis palette).

Cell cycle scoring (multiome)

Cell cycle phases were assigned using the CellCycleScoring function in Seurat. Phase-specific scores were calculated based on canonical markers,[105] and cells were assigned to G1, S, or G2/M phases. Proportions were quantified per cluster.

Integrated motif analysis and biophysical deconvolution

To systematically identify transcriptional drivers of the chromatin-accessibility shift in GCM1-deficient organoids, we performed a multi-step analysis focusing on the cytotrophoblast population, excluding terminally differentiated clusters to avoid confounding effects. We first quantified genome-wide transcription factor activity changes using chromVAR. To ensure biological relevance, candidate TFs were filtered based on RNA expression, retaining only those with detectable transcript levels (average SCT >0.1). Differentially accessible regions were identified using logistic regression, controlling for total ATAC counts as a latent variable. Peaks were classified as "Gained" (upregulated in GCM1 KO) or "Lost" (downregulated in GCM1 KO), and motif enrichment analysis was performed using FindMotifs. We defined a Target Preference score as the $\log_2$ ratio of motif enrichment in Gained versus Lost peaks. TFs were then classified into functional categories—Global Activators showing increased activity targeting newly accessible regions and Lost Drivers showing decreased activity associated with lost regions—by integrating global activity shifts with target site preference. To determine the biophysical mechanism underlying chromatin remodeling, we performed high-resolution genomic footprinting using Signac. Tn5 insertion bias was corrected based on local hexamer sequence composition. Aggregate footprint profiles were deconvolved into two distinct metrics: TF Occupancy, calculated from the central footprint region as the difference in valley depth between Control and KO, where positive values indicate reduced binding in KO; and Local Chromatin Accessibility, calculated from the flanking regions, where positive values indicate increased accessibility in KO. By plotting these metrics, we distinguished Pioneer factors exhibiting simultaneous increase in binding and flanking accessibility from Collapsed factors showing concurrent loss of binding and chromatin closure. Aggregate footprint profiles for representative factors were visualized to validate these classifications.

Reconstruction of gene regulatory networks

To map the downstream regulatory hierarchy driven by the identified Pioneer factors, we constructed a directed gene regulatory network using igraph and ggraph. Motif occurrences of these TFs were scanned within *GCM1* KO-specific accessible peaks using motifmatchr, and peaks were linked to their nearest genes using the ClosestFeature function in Signac. To isolate the active ectopic program, the network was filtered to include only target genes significantly upregulated in *GCM1* KO organoids ($\log_2$ fold change >0.25, adjusted $p < 0.05$). The network layout was computed using the Fruchterman-Reingold algorithm to visually separate distinct regulatory modules. Target node color intensity reflects RNA expression fold change in *GCM1* KO relative to Control.

Peak-gene linkage and regulatory analysis

Differentially accessible regions (DARs) between samples were identified using FindMarkers on the ATAC assay with logistic regression, controlling for total ATAC counts as a latent variable (min.pct = 0.05, logfc.threshold = 0.25). Peak-to-gene linkages were computed using LinkPeaks,[72] correlating chromatin accessibility with gene expression across cells. Genomic coverage plots were generated using CoveragePlot for regions of interest, extending 2–10 kb upstream and downstream to capture regulatory elements.

Integration of motif accessibility and gene expression

For selected transcription factors, chromVAR deviation scores were paired with target module expression scores (calculated using AddModuleScore) on a per-cell basis. The relationship between motif accessibility and target expression was visualized using scatterplots with LOESS regression lines to highlight genotype-specific trends (Control vs. *GCM1* KO). Additionally, motif accessibility dynamics along the differentiation trajectory were visualized by plotting chromVAR scores against pseudotime.

Primitive endoderm marker analysis

To assess whether ectopic *GATA6* activation was accompanied by induction of the canonical primitive endoderm (PrE) regulatory network, we examined expression of *GATA6* and its developmental partners (*GATA4*, *SOX17*, *FOXA2*, *HNF4A*, *PDGFRA*). *GCM1* KO cells were stratified based on *GATA6* expression: *GATA6*-positive (SCT-normalized expression >0) and *GATA6*-negative (expression = 0). Expression patterns were visualized using the DotPlot function in Seurat, with dot size representing the percentage of expressing cells and color intensity indicating average scaled expression.

Acquisition of hTOr-conditioned medium (hTOr-CM)

On day 8 of hTOr culture, the medium was replaced with fresh ECSY+BF (BMP4/FGF2) medium. After 72 h (on day 11), the conditioned medium was collected, centrifuged at 3000 × g for 5 min to remove cell debris. As a control, ECSY+BF medium was simultaneously cultured for 72 h in a ClinoStar bioreactor (CelVivo) under identical rotational conditions without hTOr and processed identically. Both hTOr-conditioned medium and control medium were aliquoted and stored at −80°C until further analysis.

LC-MS/MS

Culture media were analyzed for steroid hormone content by ASKA Pharmaceutical Co., Ltd (Tokyo, Japan) using liquid chromatography-tandem mass spectrometry (LC-MS/MS) with solid-phase extraction and chemical derivatization. Isotope-labeled internal standards were used for quantification, and two complementary derivatization strategies were employed: picolinyl ester derivatization for steroid hormones including estrone, estradiol, pregnenolone, and cortisol, and oxime derivatization for progesterone, 17-hydroxyprogesterone, and androstenedione.

Proteomic analysis

Proteomic profiling of hTOr-conditioned medium was performed by Proteobiologics Co., Ltd. (Osaka, Japan). Briefly, collected supernatants underwent albumin depletion, followed by protein digestion using a Lys-C/trypsin mixture. The resulting peptides were analyzed by nanoLC-MS/MS using a Q Exactive mass spectrometer (Thermo Fisher Scientific) operating in data-independent acquisition (DIA) mode. Raw data were processed using DIA-NN software (v1.8.1)[91] against the UniProtKB Human reference database with a peptide and protein false discovery rate (FDR) of <1%. For downstream functional evaluation, including rank-abundance plotting and proteomics-informed NicheNet analysis, the quantified protein intensities were $\log_2$-transformed.

Quantification of human chorionic gonadotropin (hCG)

The secretion of hCG by trophoblast organoids was quantified using a commercially available hCG ELISA Kit (Abnova, Cat# KA4005). Briefly, hTOr-conditioned medium was collected as described above, and the assay was performed according to the manufacturer's instructions. Absorbance was measured using a microplate reader, and hCG concentrations (mIU/mL) were calculated based on a standard curve generated from the reference standards provided with the kit.

3D Co-culture assays

hEMO, including GFP-expressing hEMO, were generated from human endometrial tissue as previously described[21] and co-embedded with day 11 hTOr in Matrigel. Co-cultures were maintained for eight days in ECSY medium and analyzed by immunofluorescence staining of frozen sections. For EVT differentiation, day 11 hTOr were embedded in Matrigel and cultured in EVT medium[12] for 14 days. For trophoblast-endothelial interaction studies, hTOr (1–2 per condition) were co-embedded with RFP-expressing HUVECs (5×10^6 cells/mL) in a type I collagen (Nitta Gelatin, Osaka, Japan):Matrigel matrix (7:3 ratio) and cultured in EVT medium for 14 days. Trophoblast-endothelial interactions were evaluated by immunofluorescence staining and 3D reconstruction analysis.

Quantification of epithelial height

To quantify the morphological response of hEMO to trophoblast contact, fluorescence images of co-cultures were acquired using a BZ-X fluorescence microscope (Keyence). Epithelial height was measured as the perpendicular distance from the basal to the apical surface of the GFP^+ hEMO layer using BZ-X Analyzer software (Keyence). Measurements were compared between hEMO regions in direct physical contact with hTOr ("Contact") and hEMO organoids not in contact with hTOr ("Non-contact").

Automated morphometric analysis of Co-cultures

Bright-field images of trophoblast-endometrial organoid co-cultures were acquired using a BZ-X810 microscope (Keyence) with a 2× Plan Apochromat objective (pixel size: 3.78 μm). Endometrial (hEMO) and trophoblast (hTOr) organoids were automatically segmented using Cellpose[90] with the cyto3 model. Organoid types were distinguished based on morphological features: hTOr were identified by larger size (area $\geq$143,000 μm^2) and lower mean intensity ($\leq$70 gray value), while smaller, higher-intensity structures were classified as hEMO. For each hEMO, the intensity ratio was calculated by dividing the mean intensity of the central region (>70% distance from edge by Euclidean distance transform) by that of the peripheral region (<30% distance from edge). Organoids with a ratio >1.0 were classified as lumen-positive (cystic), while those $\leq$1.0 were classified as lumen-negative (thickened/solid). Lumen retention rate was calculated as the percentage of lumen-positive organoids within defined distance bins from the nearest hTOr (Near: $\leq$1 mm, Mid: 1–2 mm, Far: >2 mm). Artifacts located >3 mm from hTOr or at Matrigel edges were excluded. Correlations were assessed using Spearman's rank coefficient, and proportion differences were tested using Fisher's exact test with Bonferroni correction.

Quantification of organoid fusion

Fusion efficiency was quantified from 3D confocal z-stacks (Zeiss LSM780×, 5× objective) using an image-processing workflow based on functions from the scikit-image library.[93] Trophoblast (KuO) and endometrial (GFP) organoids were segmented by intensity thresholding (95th percentile of non-zero voxels), followed by morphological closing, hole filling, and volume filtering (hTOr $>5 \times 10^5$ μm^3; hEMO $>1 \times 10^5$ μm^3). Contact pairs were identified by dilating trophoblast masks by 15 μm (using an anisotropic structuring element) and detecting intersection with endometrial masks. Fusion was defined by two metrics: (1) Volumetric Overlap Ratio (intersection volume/volume of smaller organoid) and (2) Fluorescence Mixing Index (mean fold-enrichment of partner signal within the mask relative to background). Pairs were classified as fused if volumetric overlap exceeded 5% and bidirectional mixing exceeded 2-fold.

Single-nucleus RNA-seq analysis of Co-culture system

Data integration and sub-clustering

Single-nucleus gene expression matrices from hEMO mono-culture, hTOr mono-culture, and co-culture samples were processed using Seurat. Data were normalized using SCTransform and integrated via the Reciprocal PCA (RPCA) workflow to correct for batch effects. Dimensionality reduction was performed using UMAP on the first 30 principal components. To ensure unbiased visualization, cell numbers were downsampled to a balanced ratio prior to projection. For lineage-specific analysis, hEMO-derived cells were computationally subsetted based on epithelial marker expression (EPCAM, PAEP) and re-clustered to identify cell states (Homeostatic, Cycling, Activated).

Pathway enrichment analysis

Differential expression analysis was performed between the Activated cluster and the Homeostatic cluster within the hEMO lineage using the FindMarkers function (Wilcoxon Rank-Sum test). The Cycling cluster was explicitly excluded from this comparison to eliminate cell cycle-dependent noise. Genes with an adjusted p-value <0.05 and $\log_2$ fold change >0.5 were used as input. Gene Ontology (GO) enrichment for Biological Processes (BP) was performed using the clusterProfiler package. Redundant terms were removed using the simplify function.

Metabolic module scoring

Metabolic pathway activity was quantified at the single-cell level using the AddModuleScore function in Seurat. Gene sets for "Oxidative Phosphorylation" and "Glycolysis" were retrieved from the MSigDB Hallmark collection. Module scores were compared between the Activated, Cycling, and Homeostatic populations using the Wilcoxon rank-sum test.

Proteomics-informed nicheNet analysis

To infer ligand-target interactions, we utilized the hTOr proteomic dataset as the "sender" ligand pool. Ligand candidates were selected by intersecting the detected secretome proteins with the NicheNet ligand-receptor database, identifying bioactive ligands (e.g., CGA, IGF2, LEP, HMGB1). Target genes were defined as the set of genes significantly upregulated in hEMO in the co-culture condition compared to the mono-culture condition (Global DEGs, adjusted $p < 0.05$). Ligand-target links were predicted using the NicheNet prior model,[92] and the regulatory potential of top-ranked ligands for key downstream targets was visualized in a heatmap.

Quantitative real-Time reverse transcriptase PCR analysis

Total cellular RNA was isolated using the RNeasy extraction kit (QIAGEN, Valencia, CA, USA). First-strand cDNA synthesis was subsequently performed with the PrimeScript II cDNA Synthesis Kit (Takara Bio). Real-time quantitative PCR analysis was conducted using a StepOnePlus Real-Time PCR System (Applied Biosystems, Foster City, CA, USA) with TB Green Premix Ex Taq II (Tli RNaseH Plus, Takara Bio), following standard manufacturer protocols. Relative target gene expression was determined via the ΔΔCt (threshold cycle) method, with glyceraldehyde-3-phosphate dehydrogenase (*GAPDH*) serving as housekeeping gene reference. All primer sequences utilized in this investigation are detailed in Table S2.

Quantitative analysis of HUVEC volume and EVT orientation

To analyze vascular remodeling and spatial relationships between extravillous trophoblasts (EVTs) and endothelial cells, 3D coordinates, segment volumes (μm^3), and orientation vectors were extracted from confocal z-stacks using Fiji (ImageJ). Coordinates were converted to physical units using the image-specific XY pixel size (0.415–0.830 μm/pixel) and a Z-step of 5.0 μm. For each HUVEC segment, the Euclidean distance to the nearest EVT was calculated.

To evaluate distance-dependent fragmentation, HUVEC segment volumes were binned in 10-μm intervals. Geometric mean volumes were plotted because segment volumes were approximately log-normally distributed. Differences between proximal (<25 μm) and distal (≥ 25 μm) segments were assessed using the Wilcoxon rank-sum test, and distance-dependent trends were visualized by LOESS regression.

For orientation analysis, the axial angle (θ) between the EVT long-axis vector (V) and the displacement vector to the nearest HUVEC structure (D) was calculated as $\theta = \arccos(|V \cdot D|/(|V| \times |D|))$, constrained to 0°–90°. Under a uniform 3D orientation, the expected mean angle is 57.3°. Observed angles were compared with this expectation using a one-sided Wilcoxon signed-rank test. Distance dependence was visualized by LOESS regression. For robustness analysis, EVTs were stratified by elongation ratio (R1/R2), and a null distribution of mean angles was generated from 10,000 random-orientation simulations. The empirical *p* value was calculated as the fraction of simulated mean angles less than or equal to the observed mean angle.

QUANTIFICATION AND STATISTICAL ANALYSIS

Statistical analyses were performed using R (v4.3.1) and GraphPad Prism (v10.0.2). Data distribution normality was assessed using the Shapiro-Wilk test to guide appropriate statistical method selection. For pairwise comparisons, two-tailed unpaired Student's t-tests or Welch's t-tests were applied, while multi-group comparisons employed one-way ANOVA with Tukey's or Dunnett's post hoc tests as appropriate. When data did not meet normality assumptions, non-parametric alternatives (Mann-Whitney U test, Wilcoxon rank-sum/signed-rank tests, and Kruskal-Wallis test with Dunn's post hoc correction) were employed. Differences between cumulative distributions were evaluated using the two-sample Kolmogorov-Smirnov test. For categorical data, differences in proportions were evaluated using Fisher's exact test with Bonferroni correction. For analyses involving clustered or hierarchical data structures, linear mixed-effects models were utilized. Directional bias was assessed by comparing observed distributions to random simulations. Results are presented as mean ± SD. For genomics analyses, multiple testing correction was applied using the Benjamini-Hochberg method with false discovery rate (FDR) < 0.05. Statistical significance was set at $p < 0.05$ unless otherwise specified. Error bars in all graphs represent standard deviation unless otherwise indicated in the specific figure legends (e.g., standard error of the mean [SEM] or standard error of proportions [SEP]). The exact values of n (representing the number of biological replicates, independent experiments, or individual organoids/cells analyzed) are detailed in the respective figure legends.